

A Solar Battery with Light Assisted Discharge and Charge Interfaces

**A thesis submitted
towards partial fulfilment of BS-MS dual degree**

By

Bhuneshwar Paswan

(Reg. No.: 20111025)

Under the guidance of

Dr. Muhammed Musthafa, IISER Pune, INDIA



To

The Department of Chemistry

Indian Institute of Science Education and Research (IISER) Pune

Pune – 411008, INDIA

DEDICATED TO MY BELOVED PARENTS AND FRIENDS....

CERTIFICATE

This is to certify that this dissertation entitled “**A solar battery with light assisted discharge and charge interfaces**” towards the partial fulfilment of the BS-MS dual degree programme at the Indian Institute of Science Education and Research, Pune represents original research carried out by “**Bhuneshwar Paswan** at IISER Pune” under the supervision of “**Dr. Muhammed Musthafa**, Assistant Professor, Department of Chemistry” IISER Pune during the academic year 2015-2016.



Dr. Muhammed Musthafa
(Supervisor)

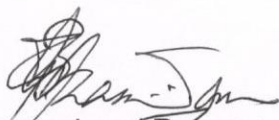
Date: 28/03/2016

Place: Pune

डॉ. मुहम्मद मुस्तफा / Dr. Muhammed Musthafa
सहायक प्राध्यापक / Assistant Professor
भारतीय विज्ञान शिक्षा एवं अनुसंधान संस्थान
Indian Institute of Science Education & Research
पुणे-411 008, भारत / Pune - 411 008, India

DECLARATION

I hereby declare that the matter embodied in the report entitled "**A solar battery with light assisted discharge and charge Interfaces**" are the results of the investigations carried out by me at the **Department of Chemistry, IISER Pune**, under the supervision of **Dr. Muhammed Musthafa** and the same has not been submitted elsewhere for any other degree.



Bhuneshwar Paswan

Reg. No.: 20111025

Date: 28th March 2016

Place: Pune

ACKNOWLEDGEMENT

I wish to express my sincere gratitude to my guide Dr. Muhammed Musthafa, Dept. of Chemistry, IISER Pune for his encouraging and valuable discussion, never failing kindness and inspiring guidance throughout the project.

I would like to thank Dr. Pattayil Joy, Dept. of Physical and Material Chemistry, CSIR-NCL, Pune for his guidance and mentorship throughout the project.

I wish to express my gratitude to post doc Dr. Ravikumar for guiding me throughout the project in conducting experiments and characterizations and provide me with fruitful suggestions.

I want to thanks Dr. Shahid Shafi for discussing my X-ray diffraction data and giving me valuable suggestions and explanations.

I would like to thank my labmate Algar Raja for assisting me in conducting cyclic voltammogram of battery electrode.

I would like to thank my lab members: Mruthyunjayachari C. D., Algar Raja, Manu Gautam, Om Shankar Tiwari and Shambulinga to help in conducting various experiments in the projects and giving valuable inputs.

I would like to thank Dr. Atul Kulkarni and his company Ionbond, MIDC, Pune for provide us with fabricated Titanium Nitride (TiNs) and IISc, Bangalore to allow us to perform X-ray photoelectron microscopy measurement on TiN.

I would like to thanks FESEM operator Mr. Anil Shetti for performing SEM and EDS of my samples.

I would like to thank IISER Pune and MHRD, govt. of India for providing me facilities and financial assistance to carry out my experiments and characterizations.

I would like to thank my friends Arun Kumar, Tapash Das, Ashish Kumar P K, Nitin Kumar, Shalini Jha, Prerna Sharma and Ankit Tiwari and my family members for their guidance and support throughout the project.

-- Bhuneshwar Paswan

CONTENTS

• Abstract	1
1. Introduction	2
1.1 Fuel cells	2
1.2 Supercapacitors	4
1.3 Solar cells	5
1.4 Batteries	6
1.5 Novelty in the context of present status	7
2. Methods	8
2.1 Experimental Section	8
2.1.1 Materials Required	8
2.1.2 Fabrication of Titanium Nitride electrode	8
2.1.3 Fabrication of battery electrode: Prussian blue analogue (PBA) on FTO coated glass	8
2.1.4 Fabrication of photocathode: Mg doped α -Fe ₂ O ₃ (MgFeO)	8
2.1.5 Characterization	9
2.1.6 Battery Architect	9
2.2 Theoretical/Computational Section	10
2.2.1 Cyclic Voltammetry	10
2.2.2 UV-vis Absorption spectroscopy	12
2.2.3 X-ray diffraction (XRD)	12
2.2.4 Kubelka-Munk Plot/ Tauc Plot	13
2.2.5 Mott-Schottky Plot	13
2.2.6 Theoretical capacity of a battery	14
2.2.7 Reference Electrode	14
2.2.8 Calculation of Valence band, Conduction band, Schottky barrier height and built-in potential	14
3. Results and discussion	17
3.1 Characterisation of battery architectural components	17
3.1.1 Characterisation of battery electrode: Prussian blue analogue	17

3.1.2	Characterisation of photoanode: Titanium Nitride	19
3.1.3	Characterisation of photoanode: MgFeO	21
3.2	Solar battery architect and charge discharge behavior	25
3.3	Stability and cycling	30
4.	Conclusions	34
5.	References	35

List of Figures

1.1	A typical PEM (proton exchange membrane) fuel cell.	3
1.2	Diagram showing various fuel cell components.	3
1.3	Ragone plot of electrochemical energy storage and conversion devices.	4
1.4	Diagram of electrolytic double layer supercapacitor (EDLS) and pseudocapacitor.	5
1.5	Schematic of a photovoltaic solar Cell.	5
1.6	A schematic of the internal processes in a battery	6
2.1	Schematic representation of solar battery operation.	10
2.2	A typical cyclic voltammogram.	11
2.3	Diagram showing X-ray diffraction from atoms of a crystal.	12
3.1	Characterisation of battery electrode.	18
3.2	Characterisation of photoanode.	20
3.3	Characterisation of photocathode.	22
3.4	FESEM and band diagram of MgFeO.	23-24
3.5	Charge discharge behavior of TiN PBA electrodes.	27
3.6	UV-vis spectra and XRD of PBA during charge chemistry with the photocathode.	28
3.7	Discharge and charge behavior of solar battery in N ₂ and O ₂ atmosphere.	29
3.8	Energy level diagram of battery electrodes.	30
3.9	XRD of TiN and photodischarge profiles for 250 cycle	

in different light conditions.	31
3.10 UV-VIS spectra and XRD of PBA and XRD of photocathode for 250 cycles during photocharge.	32
3.11 Charge profiles of the solar battery for 250 cycle in different light conditions.	33

List of Tables

2.1 Instruments specification for different physicochemical techniques.	9
3.1 Semiconductor relevant characteristics of battery electrodes.	24
3.2 Atomic % of Mg in electrodeposition solution compared with the EDS data.	24

ABSTRACT

Energy is the one of the decisive tool for survival of human civilization, which is harvested from various sources, among which fossil fuels occupy a larger space. The major problems which comes from the enormous use of fossil fuels are that they cause excessive pollution to air, water and land and increase the accumulation of greenhouse gases in the ecosystem, threatening the lives various flora and fauna thriving on this planet. In this context harvesting and storing solar energy by artificial photosynthesis and certain electrochemical reactions in batteries gain paramount importance. Latter technology requires two separate devices as a part of the solar energy harvesting architect, for eg, a solar cell to harvest light and a battery to store it, demanding complex engineering design with multiple interfaces. In this project the properties of batteries and solar cells are integrated in to a single device called “Solar Battery”, which in turn can harvest and store energy in the same device. The proposed battery consists of a titanium nitride (TiN) photoanode as the discharge component, Prussian blue analogue (PBA) electrode as battery active species and Mg doped- Fe_2O_3 (MgFeO) photocathode as the charge component. The result indicate that the battery can be cycled in ambient, visible and UV-vis light without the aid of any external power supply and the architectural components possess decent stability and cyclability. The advantage of the present architect is that both discharge and charge reactions are light assisted, considerably simplifying the discharge and charge chemistry from the kinetic limitations of active metal ions dissolution/ redeposition, dendrite formation and associated safety issues. The discharge mechanism is identified as O_2 evolution at the photoanode with concomitant metal ion insertion at the PBA electrode. The charge chemistry involves the pumping of electrons from the reduced PBA to the photocathode with simultaneous H_2 evolution at the semiconductor/electrolyte interface. As the charge reaction is light assisted, it resulted in charging the battery without any external bias, ultimately leading to a complete solar battery.

1. INTRODUCTION

Energy plays a vital role in human survival and day-to-day accomplishment of work. For these, various energy sources such as fossil fuels, wind energy, tidal energy, geothermal, solar energy etc., have been exploited. Internal combustion engines emit tons of carbon oxides, nitrogen oxide and other toxic substances into the atmosphere causing severe pollution and global warming^{1,2}. Polar ice cubes have already started melting and if all the ice melts at the present pace, in the foreseeable future the entire earth and the life it stands for will be engulfed by the soaring oceans. Oceans can be a sink for CO₂ and its increased accumulation has already lowered the pH levels in certain areas, threatening the lives of shell fish and other aquatic species existing in those ecosystems³⁻⁶. In this context, during the UN conference on climate change, held Paris on Dec 2015 world leaders have unanimously agreed to limit the global warming temperature to 1.5 °C (http://unfccc.int/meetings/paris_nov_2015/meeting/8926.php). In order to achieve this goal zero emission technologies have to be developed at least by 2050. Electrochemical energy storage and conversion devices such as batteries, fuel cells, supercapacitors and solar cells are potential zero emission technologies as explained below.

1.1 Fuel cells

Fuel cells are electrochemical energy conversion devices that convert chemical energy directly into electricity (figure 1.1). Proton exchange membrane fuel cells (PEMFC) works using hydrogen and oxygen fuels and generate water which can be used for drinking and/or irrigation purposes. With cogeneration technique i.e. using both electricity and heat generated from it, their efficiency can be reached up to 90% ⁷. But fuel cells have a complex design and structure and its operation require a sophisticated system, with expensive platinum nanoparticles and Nafion membrane (figure 1.2). Scientific exploration are going on to minimize and optimize these parameters and to design cost effective and economical fuel cell systems. Also the production, storage and transportation of explosive hydrogen gas is a big hurdle. For these reasons the electricity produced from a fuel cell is always expensive compared to internal combustion engines,

however one factor that forces everyone to embrace this technology is its cleaner energy output without threatening the lives on this planet in any way.

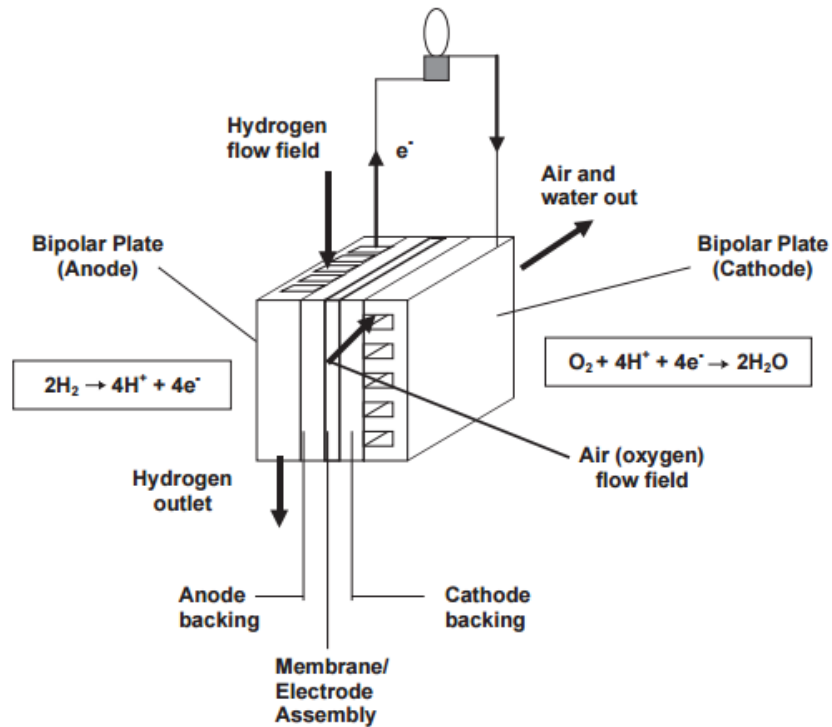


Figure 1.1 : A typical PEM (proton exchange membrane) fuel cell. (A. Hermann et al. / *International Journal of Hydrogen Energy* 30 (2005) 1297 – 1302)

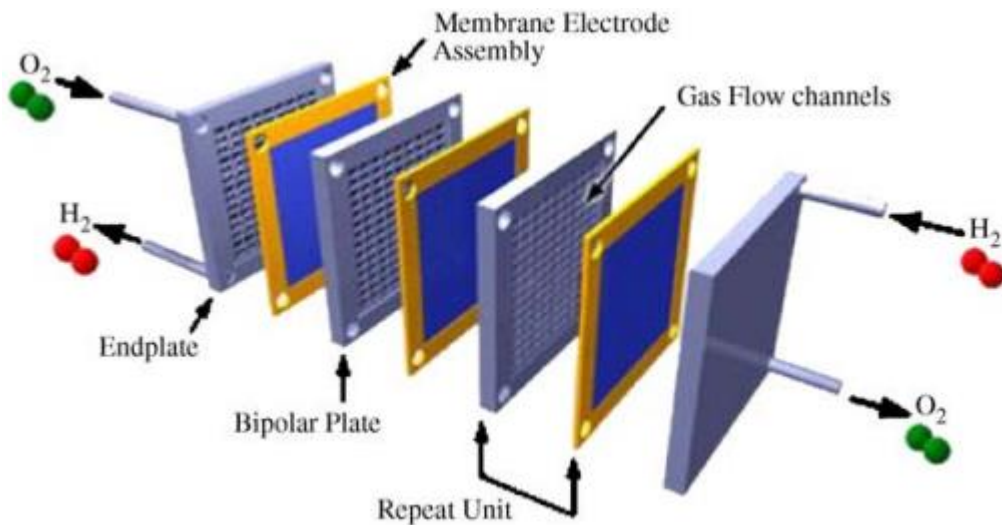


Figure 1.2 : Diagram showing various fuel cell components. (X. Li, I. Sabir / *International Journal of Hydrogen Energy* 30 (2005) 359 – 371)

1.2 Supercapacitors

Electrochemical supercapacitors were first invented in 1957. Batteries and fuel cells have high energy densities but low power density (figure 1.3). For applications demanding high power, batteries and fuel cells can't be used. However supercapacitors can provide higher power in short time as shown in the Ragone plot (figure 1.3) and therefore they are integral part in hybrid electric vehicles⁸.

A supercapacitor is a potential zero emission technology and it has got two conducting plates separated by a dielectric medium (figure 1.4). It can store electrical energy in the form of charge on current collectors. There are two types of supercapacitors, electrochemical double layer supercapacitors and pseudocapacitors. In electrochemical double layer supercapacitors physical adsorption/desorption of ions take place at the interfaces on the electrode surface and they are essentially non-Faradaic in nature. In pseudocapacitors a surface bound redox reaction governs charge storage.

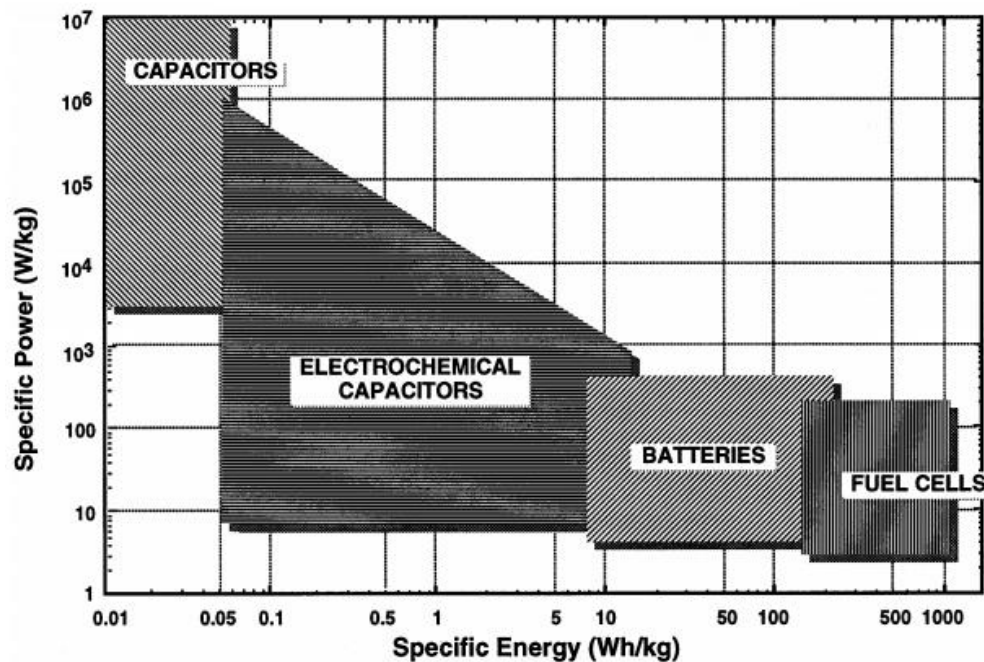


Figure 1.3. : Ragone plot of electrochemical energy storage and conversion devices. (R. Kotz, and M. C. (1999). *Principles and applications of electrochemical capacitors. Electrochimica Acta*, 45(45), pp. 2483–2498)

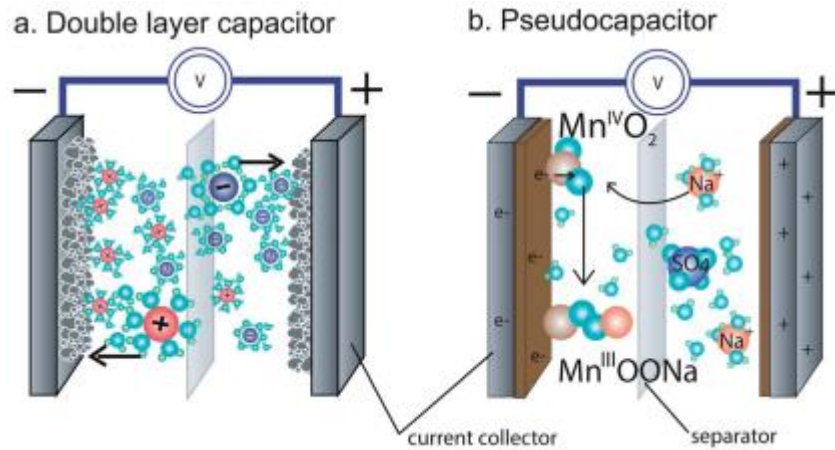


Figure 1.4: Diagram of (a) electrolytic double layer supercapacitor (EDLS) and (b) pseudocapacitor. (*J. Mater. Chem. A*, 2014, 2, 10776).

1.3 Solar cells

There are several types of solar cells: photovoltaics (PV), dye-sensitized solar cells, perovskite solar cells, organics solar cells, etc⁹. In PV solar cells (figure 1.5) photons fall at the p-n junction and electron-hole pairs will be created. The electrons thus pass through the external circuit and then combine with the holes moving towards p-type region. This motion of electrons cause electricity which can be used to charge either a battery or to power an external load. Generally n-type and p-type silicon materials are used for making a p-n junction. A solar cell always require a battery to store the energy harvested by the solar cell for later use, thus introducing multiple junctions and interfaces with associated kinetics and safety issues.

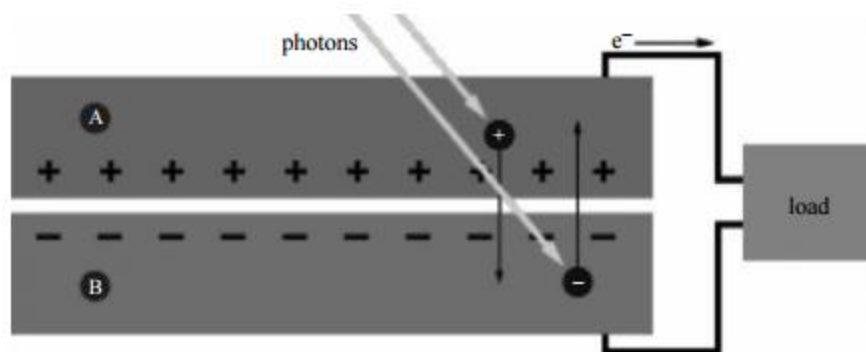


Figure 1.5 : Schematic of a photovoltaic solar Cell. (*Phil. Trans. R. Soc. A* (2007) 365, 993–1005)

1.4 Batteries

Batteries are mainly divided into two types: primary and secondary. Primary batteries convert chemical energy into electricity and when all the components are exhausted battery stops functioning. Secondary batteries can be used multiple times, by charging externally. During discharge chemical energy is converted into electricity (figure 1.6). During the charge electrical energy is stored as chemical energy which can be converted back to electricity when required (figure 1.6).

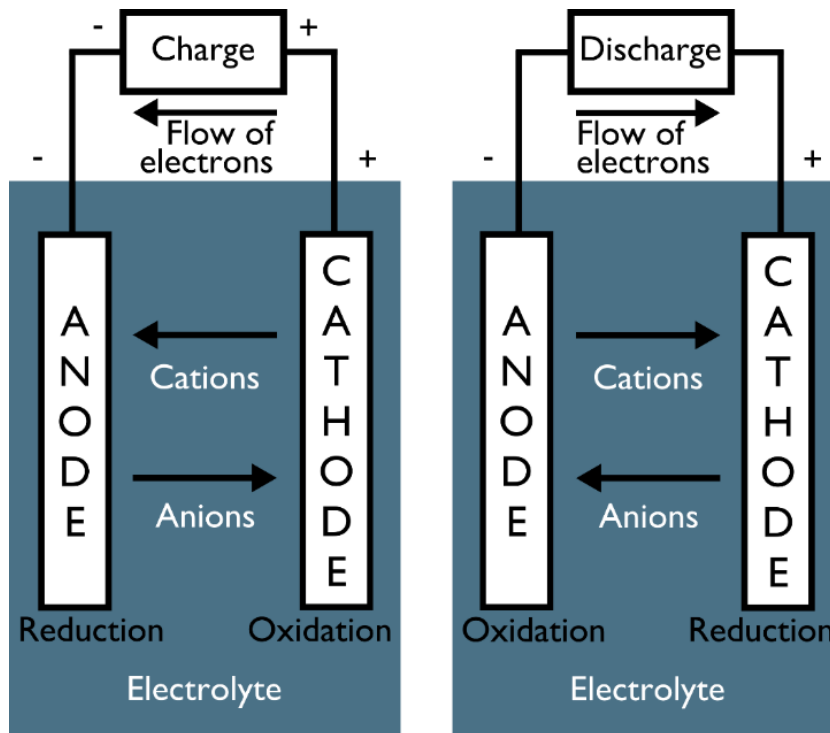


Figure 1.6: A schematic of the internal processes in a battery during charge and discharge. (Hebrink, T. J. *Durable Polymeric Films for Increasing the Performance of Concentrators*. In *Third Generation Photovoltaics*; Fthenakis, V., Ed.; InTech: Rijeka, Croatia, 2012; Chapter 8. ISBN: 978-953-51-0304-2.)

Typically a battery has three components: anode, cathode and an ionically conducting electrolyte which is in contact with both electrodes. Electrolyte contains anions and cations. During discharge oxidation takes place at the anode and the cations from electrolyte move to the cathode causing a reduction reaction with the electrons reaching

the cathode through the external circuit and the process gets reversed during the charge chemistry where electricity from an external source is pumped into the battery¹⁰. Discharge is a spontaneous process while charge is a non-spontaneous process in which electrons flow is reversed by supplying energy more than the thermodynamic voltage of the battery.

1.5 Novelty in the context of present status

A solar energy harvesting module will always have a secondary battery storage unit to store the energy harvested for later use⁹. The requirements of separate modules to harvest and store introduce multiple electrode components and junctions with complicated solution and electrode chemistries and associated kinetic and efficiency issues.

Here we show a solar battery architect by combining energy harvesting and storing components in the same device which is more economical and practical. The assembly consists of a three electrode configuration with a titanium nitride photoanode discharge component, promising metal ion insertion battery electrode belonging to the Prussian blue Analogue family (PBA) and Mg doped α -Fe₂O₃ (MgFeO) photocathode charging component. Titanium nitride photoanode can be a potential negative electrode for aqueous rechargeable batteries without having the stability and safety issues usually encountered in metal ion batteries. By bringing in a MgFeO photocathode that can absorb the light in the region where solar power is intense, we have successfully achieved ambient light assisted charging of aq. rechargeable batteries. The advantage of the present architect is that both discharge and charge reactions are light assisted, considerably simplifying the discharge and charge chemistry from the kinetic limitations of active metal ions dissolution/ redeposition, dendrite formation and associated safety issues. As the charge reaction is light assisted, it resulted in charging the battery without any external bias ultimately leading to a complete solar battery.

2. METHODS

2.1. Experimental Section.

2.1.1 Materials Required:

Potassium chloride (assay 99.8%, Rankem), potassium fluoride (assay 99%, Rankem), magnesium chloride hexahydrate (assay 99%, Sigma Aldrich), hydrogen peroxide (35% w/w aq. solution, Alfa Aesar), iron(III)chloride anhydrous (assay 98%, Alfa Aesar), potassium hexacyanoferrate(III) (assay 99%, Alfa Aesar) and fluorine doped-tin oxide (FTO) coated glass (Dyesol company) were used as received.

2.1.2 Fabrication of Titanium Nitride electrode:

Biased Physical Vapour Deposition technique was used to deposit titanium nitride on stainless steel (SS304 grade) substrate (thickness 0.15 mm). For this a titanium plate was used as a source of titanium and a vacuum of 10^{-6} Torr was created before deposition in the chamber used for deposition. Reactive nitrogen gas pressure was kept at 10mTorr during the deposition of TiN and the substrate voltage was ~ 200 V. TiN thickness on stainless steel was found to be 2–3 μm . UV-vis absorbance measurement, XRD, Mott-Schottky and XPS measurement were performed to ensure the formation of TiN layer on SS304.

2.1.3 Fabrication of battery electrode: Prussian blue analogue (PBA) on FTO coated glass:

A solution of 20 mM ferric chloride and 20 mM potassium ferrocyanide and 100 mM KCl was prepared. Prussian blue was electrodeposited on 2cmX2cm FTO coated glass by applying a current of ~ 300 microampere for 150 sec¹¹. After this it was gently rinsed with water and dried in ambient light.

2.1.4 Fabrication of photocathode: Mg doped α -Fe₂O₃ (MgFeO)

A 40 mL solution consisting of 5 mM FeCl₃ + 5 mM KF + 0.1 M KCl + 1 M H₂O₂ was prepared. Fluoride was added to decrease the reduction potential of Fe³⁺ to Fe²⁺ and the KCl was used as a supporting electrolyte^{12,13}. H₂O₂ has dual functions : firstly it produces OH⁻ ions during the reduction process so that the pH in the immediate vicinity of the working electrode increases, aiding the electrodeposition of iron hydroxides; secondly it stabilize the dopant-precursor in aq. solution. Magnesium chloride was used

as precursor for Mg doping with molar ratio $[Mg/(Mg+Fe)]$ in the range from 0% to 25%. Cyclic voltammogram was performed at a scan rate of 200 mV/sec from -500mV to 410 mV Vs Ag/AgCl (3M KCl) for 30 cycles to electrodeposit Mg doped α -Fe₂O₃ on FTO coated glass. Electrodes were gently washed with water and then calcinated at 600 °C for 4hrs. For calcination, the ramp time to reach to 600 °C from 30 °C was 4.75 hrs and soak time was 4 hrs at 600 °C. The system was allowed to cool down to 30 °C from 600 °C in 4.75 hrs.

2.1.5 Characterisation

Various electrodes and battery architect were thoroughly characterised by different physicochemical techniques as detailed below.

Table 2.1: Instruments specification for different physicochemical techniques.

<u>S. No</u>	<u>Technique</u>	<u>Machine</u>	<u>Company</u>	<u>Model</u>
1	UV-VIS Spectroscopy	Spectroscan UV 2600	ThermoFisher Scientific	UV 2600
2	Calcination	Nabertherm more than 30-3000 °C	Nabrtherm	SN219255
3	CV, Cycling data and Electrodeposition	Basi-Epsilon-EC	Epsilon	LC Epsilon
4	FESEM & EDS	Zeiss FESEM	Zeiss	Ultra Plus 4095
5	XRD	D8 Advance	Bruker	A18-A1 204974

2.1.6 Battery Architect

Proposed solar battery architect was fabricated using, TiN as photoanode, MgFeO as photocathode and PBA as the battery electrode (figure 2.1). After the discharge of photoelectrode and battery electrode, the battery active species was regenerated by short circuiting to the photocathode.

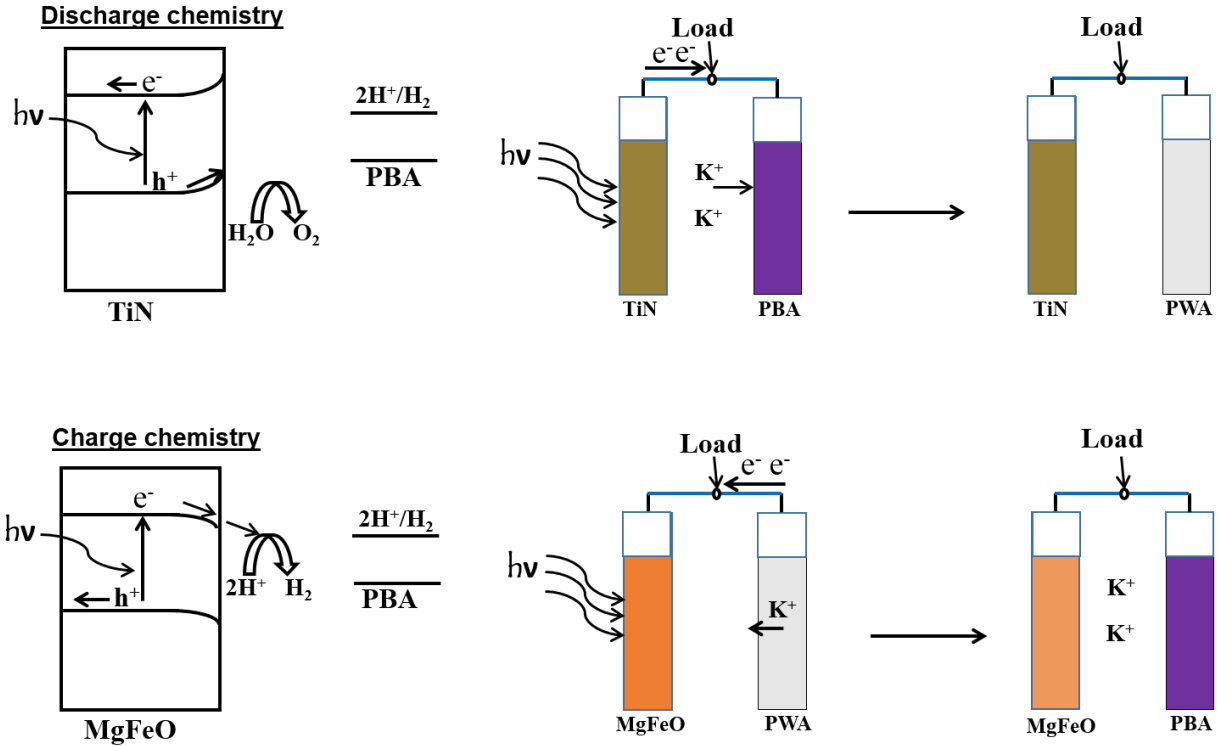


Figure 2.1: Schematic representation of solar battery operation.

2.2. Theoretical/Computational Section

2.2.1 Cyclic Voltammetry

In cyclic voltammetry technique, a potential is applied to the working electrode from an initial value V_i to final value V_f (known as switching potential) immersed in an electrolyte solution and the current response is measured (figure 2.2). The potential range $V_i - V_f$ is known as the potential window in which the material is supposed to show a redox behaviour. At switching potential the scan gets reversed. The potential of the working electrode is controlled and measured with respect to the reference electrode. The response current is then plotted as a function of applied potential¹⁴. The electron transfer rate constant for a reduction process is a function of potential is given by the Butler/Volmer equation

$k_f = k_0 \cdot \exp\left\{\frac{-\alpha n F}{RT}(E - E_0)\right\}$ - (2.1), where k_0 is the standard rate constant of the electrochemical reaction, F is Faraday constant, R is universal gas constant, T is

Temperature, n is number of electron transferred, α is the symmetry factor, E is the applied electrode potential and E_0 is the formal potential.

Similarly the electron transfer rate for the reverse process is given by.

$$k_f = k_0 \cdot \exp \left\{ \frac{(1-\alpha)nF}{RT} (E - E_0) \right\} \quad - (2.2)$$

The cyclic voltammogram is used to determine the formal reaction potential by taking the average of anodic peak potential E_{PA} and cathodic peak potential E_{PC} i.e.

$$E_0 = \frac{E_{PA} + E_{PC}}{2} \quad - (2.3)$$

This is an approximation which will be accurate when electron transfer is reversible and the diffusion coefficient of reduced and oxidised forms are same. In a reversible process the concentration of oxidised and reduced form must be in equilibrium with each other on the electrode surface. The equilibrium ratio at a given potential is given by Nernst Equation :

$$E = E_0 - \frac{RT}{nF} \ln \left(\frac{[R]}{[O]} \right) \quad - (2.4)$$

Here [O] is oxidised form and [R] is the reduced form.

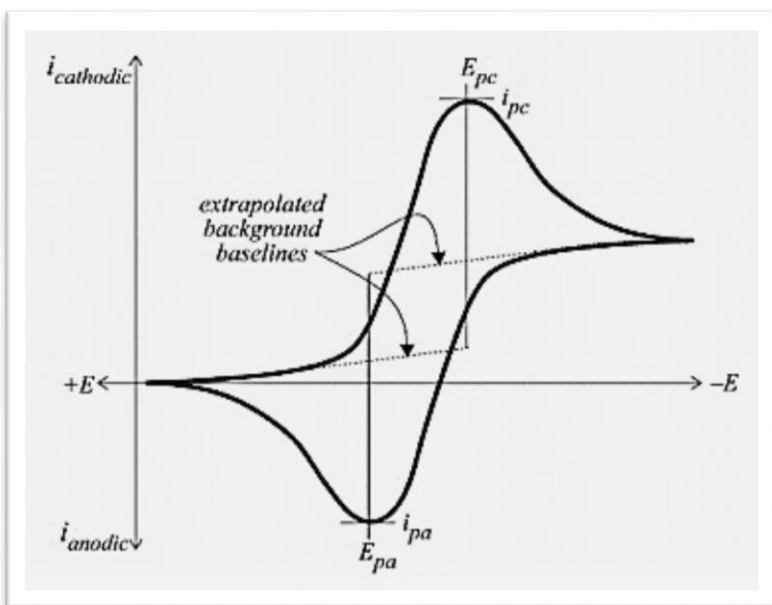


Figure 2.2: A typical cyclic voltammogram.

2.2.2 UV-vis Absorption spectroscopy

UV-vis spectroscopy is used to determine how much amount of light is absorbed, transmitted or reflected by any material. Beer-Lambert's law suggests that the absorbance is directly proportional to path length l and concentration of the sample c ¹⁵.

$$A = \log_{10} \left(\frac{I_0}{I} \right) = \epsilon cl \quad \text{(2.5)}$$

where ϵ is the constant of proportionality also called absorptivity, I_0 is the intensity of incident light and I is the transmitted light intensity.

2.2.3 X-ray diffraction (XRD)

XRD is a diffraction technique generally used to determine the crystal structure of a crystalline material in which the constituent atoms cause a beam of incident X-rays to diffract into many specific directions (figure 2.3)¹⁶. When X-ray falls on a crystalline material, it is scattered by its atoms primarily through its electrons. Constructive interference make the scattered waves to remain in phase if the path length of each wave is an integer multiple of the wavelength. Constructive interference condition on the scattering angle θ is described by the Bragg's equation: $2d \sin \theta = n\lambda$ - (2.6)

Where , θ is the scattering angle, n is a +ve integer, λ is the wavelength of the X-ray beam and d spacing between diffracting planes.

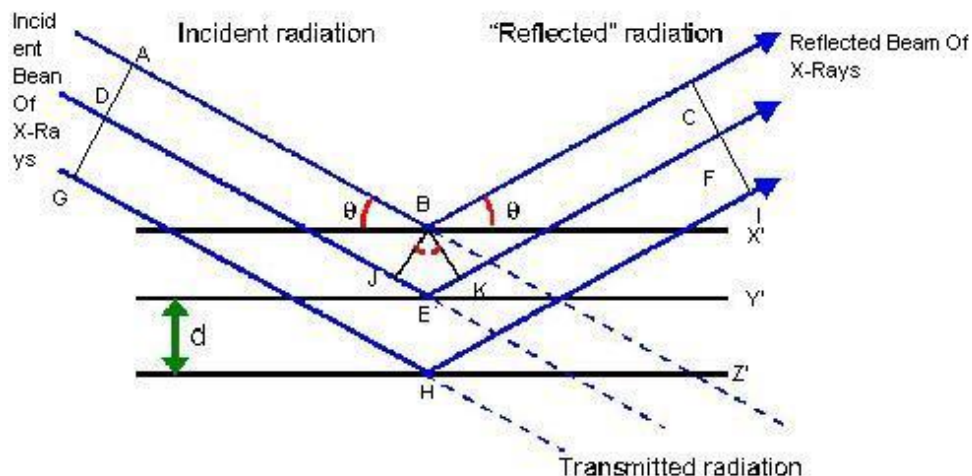


Figure 2.3: Diagram showing X-ray diffraction from atoms of a crystal (<http://wesharepics.info/imagexgkl-x-ray-diffraction.asp>).

2.2.4 Kubelka-Munk Plot/ Tauc Plot

It is used to determine the optical band gap or Tauc gap of any semiconductor from its absorbance spectra using the following Tauc equation^{17,18}.

$$(\alpha h\nu)^{1/n} = A(h\nu - E_g) \quad - (2.7), \text{ where}$$

$$n = \begin{cases} \frac{1}{2}, & \text{Direct allowed transitions} \\ 2, & \text{indirect allowed transitions} \\ \frac{3}{2}, & \text{direct forbidden transitions} \\ 3, & \text{indirect forbidden transitions} \end{cases}$$

h is Plank's constant, E_g is the optical band gap, ν is frequency, and α is absorption coefficient and is determined by the formula:

$$\alpha = \frac{-2.303 \log(T)}{d} = \frac{4\pi k}{\lambda} \quad - (2.8)$$

where T is the transmittance, ($T = 10^{-A}$, where A is absorbance) d is the thickness of the film, λ is the wavelength and k is the extinction coefficient. In the equation 2.7, A is a constant that depends upon refractive index of the material, reduced mass, Plank's constant, fundamental unit of charge and speed of light.

2.2.5 Mott-Schottky Plot

Mott-Schottky plot is used to determine the carrier density in any semiconductor and its flat-band potential or Fermi energy level. They can be determined by the following equation^{19,20}.

$$\frac{1}{C_{SC}^2} = \frac{2}{e\epsilon_0\epsilon_r N_A} \left(U - U_{fb} - \frac{k_B T}{e} \right) \quad - (2.9)$$

k_B is Boltzmann constant, T is Kelvin temperature, e is the fundamental unit of charge, ϵ_0 is absolute permittivity, ϵ_r is relative permittivity, N_A is acceptor/donor density and C_{SC} is space-charge capacitance.

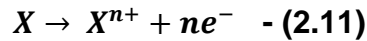
From plotted graph, the extrapolation of the linear part to the X-axis to the point where $\frac{1}{C_{SC}^2} = 0$ will give flat band potential of the material. Slope of the line can provide information on the carrier density through the following equation:

$$m = \left| \frac{2}{e\epsilon_0\epsilon_r N_A} \right| - (2.10)$$

which is deduced from Mott-Schottky equation 2.9. The slope is positive for n-type semiconductors and negative for p-type semiconductors.

2.2.6 Theoretical capacity of a battery

Considering an ion X of battery electrode undergoing oxidation or reduction reaction:



The theoretical capacity ξ of a battery is given by the following equation:

$$\xi = \frac{nF}{3600M} - (2.12)$$

where n is no. of electrons/ions transferred per mole of the reaction, F is Faraday constant and M is molecular weight/ molar mass (g/mol).

2.2.7 Reference Electrode

A reference electrode is an electrode having well-known and stable electrode potential. Below are the commonly used reference electrodes with their potentials vs standard hydrogen electrode (SHE):

- Standard Hydrogen Electrode (SHE) ($E=0$) activity of $H^+ = 1$
- Reversible Hydrogen Electrode (RHE) ($E = 0.000 - 0.059 \cdot \text{pH}$)
- Silver-Silver chloride electrode ($Ag/AgCl$) ($E = +0.197$, KCl saturated)

2.2.8 Calculation of Valence band, Conduction band, Schottky barrier height and built-in potential

In the present solar battery, TiN was used as photoanode which is an n-type semiconductor and Mg doped $\alpha\text{-Fe}_2\text{O}_3$ ($MgFeO$) was used as photocathode which is a p-type semiconductor. For the calculation of above mentioned parameters following physical quantities were used:

Fundamental unit of charge, $e = 1.602 \times 10^{-19} \text{C}$

Absolute permittivity, $\epsilon_0 = 8.8542 \times 10^{-12} \text{J}^{-1} \text{C}^2 \text{m}^{-1}$

Relative permittivity, $\epsilon_r = \begin{cases} 4.5, TiN \\ 80, MgFeO \end{cases}$ (ref. 21,22)

Mass of Electron, $m_e = 9.11 \times 10^{-31} \text{ kg}$

Boltzmann constant, $K_B = 1.381 \times 10^{-23} \text{ JK}^{-1}$

Plank's constant, $h = 6.62608 \times 10^{-34} \text{ Js}$

Area of electrode during Mott – Schottky measurement, $A = \begin{cases} 0.04 \text{ cm}^2, \text{TiN} \\ 0.071 \text{ cm}^2, \text{MgFeO} \end{cases}$

Kelvin Temperature, $T = 298 \text{ K}$

For TiN, effective mass of an electron, $m_e^* = 1.1 m_e$ ²³

For MgFeO, effective mass of a hole, $m_h^* = 2.1 m_e$ ²⁴

Using above physical quantity semiconductor parameters of TiN and MgFeO has been calculated.

Donor-density and flat band potential of TiN and MgFeO were calculated from Mott-Schottky plot and their band gaps were estimated from Tauc Plot^{19,20}.

The Density of states of MgFeO and TiN were calculated from the following equations

$$\text{Density of states} = \begin{cases} N_C = 2 \left(\frac{2\pi m_e^* K_B T}{h^2} \right)^{3/2}, \text{ for TiN} \\ N_V = 2 \left(\frac{2\pi m_h^* K_B T}{h^2} \right)^{3/2}, \text{ for MgFeO} \end{cases} \quad \text{-(2.13)} \quad \text{(ref. 25)}$$

Once the density of states of TiN is calculated, its conduction band E_C and hence valance band E_V is calculated using equations 2.14 & 2.16²⁶:

$$E_C = E_{FB} + \frac{K_B T}{e} \ln \left(\frac{N_D}{N_C} \right) \quad \text{-(2.14)}$$

Suppose this gives us x potential in V, then its conversion from V to eV can be calculated by using following equation²⁶:

$$E_C = [-4.44 - (x)] \text{ in eV} \quad \text{-(2.15)}$$

and the valance band position is given by²⁶:

$$E_V = (E_C - E_G) \text{ in eV} \quad \text{-(2.16)}$$

Similarly, the valance band E_V and conduction band E_C of MgFeO is calculated by the following equations²²:

$$E_V = -E_{FB} + \frac{K_B T}{e} \ln \left(\frac{N_A}{N_V} \right) \quad \text{-(2.17)}$$

$$E_V = [-4.44 + x] \text{ in eV}; E_C = (E_V + E_G) - \text{(2.18)}$$

After calculating these parameters the depletion layer width W_{dep} in which band bending takes place was calculated by the following equation²⁰:

$$W_{dep} = \left(\frac{2\varepsilon_0\varepsilon_r}{eN_D} \right)^{1/2} \left[U - U_{fb} - \frac{k_B T}{e} \right]^{1/2} - \text{(2.19)}$$

Calculation of built-in potential φ_{bi} which is the potential across the depletion layer which is in thermal equilibrium is obtained by equation 2.20²⁰:

$$\varphi_{bi} = \frac{W_{dep}^2 e N_D}{2\varepsilon_0\varepsilon_r} - \text{(2.20)}$$

The Schottky-barrier height, φ_{bn} which is the potential energy barrier formed at semiconductor electrolyte junction, is related by the following equation²⁶:

$$\varphi_{bn} = \begin{cases} (E_C - E_{FB}) + \varphi_{bi}, & \text{for TiN} \\ (E_{FB} - E_V) + \varphi_{bi}, & \text{for MgFeO} \end{cases} - \text{(2.21)}$$

3. RESULTS AND DISCUSSION

3.1 Characterisation of battery architectural components

3.1.1 Characterisation of battery electrode: Prussian blue analogue

Cyclic voltammogram (CV) of Prussian blue analogue (PBA) deposited on Glassy carbon (GC) electrode, figure 3.1a, shows two pairs of redox peaks centered at 0.37 V and 1.05 V with respect to SHE and the associated reactions are shown in equations 3.1 and 3.2 and it consists of metal ion insertion/deinsertions with concomitant redox reactions of high spin and low spin transition metal ions^{27,28}. As shown, the redox chemistry is dominated by the insertion/deinsertion of metal ions with minimal structural changes making it a promising battery electrode material. Multiple cycling, figure 3.1b, did not demonstrate hysteresis in redox currents or potentials suggesting the battery electrode is stable under extended cycling. XRD pattern, figure 3.1c, shows the face centered cubic lattice of battery electrode belonging to the PBA family^{29,30}. Due to their open framework structure these materials can undergo metal ion intercalation/deintercalation for maintaining the charge neutrality making them inexpensive and environmentally benign insertion cathode and anode materials for designing rechargeable batteries^{29, 31,32}. UV-vis spectrum, figure 3.1d, during the reduction and oxidation suggest their electrochromic behavior from opaque to transparent state due to intervalence charge transfer, confirming the redox behavior mainly stemming from the electrochemistry of transition metal ions. Further the digital photographs, figure 3.2e, of FTO coated PBA shows a blue colour for the oxidized state in contrast to a colorless state for the reduced form suggesting their redox energies can be deciphered from physical appearance. In essence the chosen battery species belonging to PBA family represents an inexpensive and environmentally benign insertion electrode possessing decent stability and cyclability for constructing aqueous rechargeable batteries.

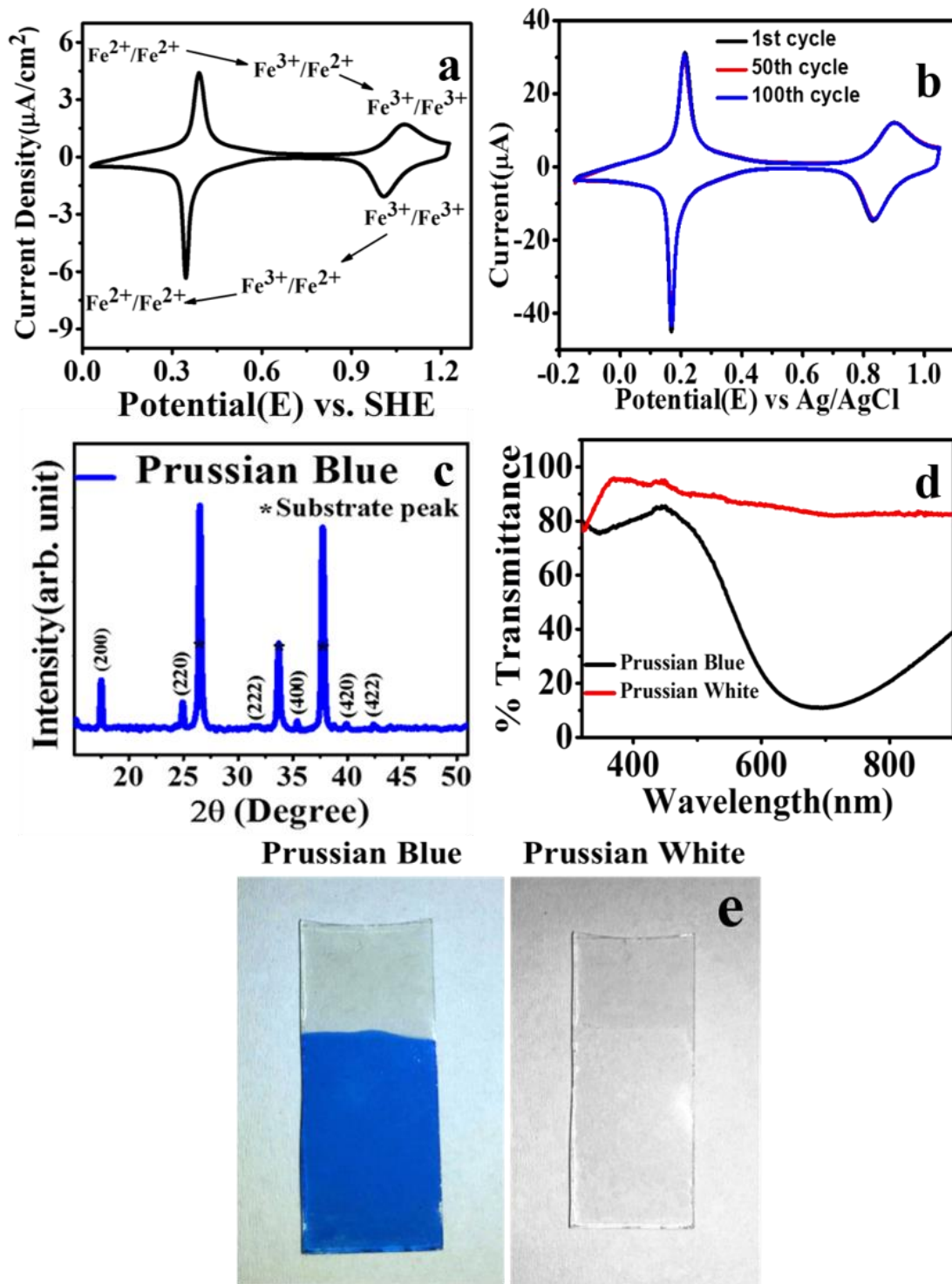
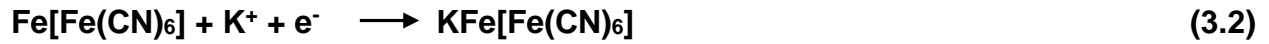
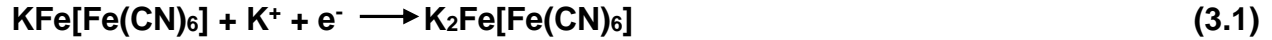


Figure 3.1. (a) Cyclic voltammogram of PBA, (b) extended cyclic voltammogram of PBA for 100 cycles, (c) XRD of PBA, (d) UV-vis spectra of PBA and its reduced form and (e) digital image of PBA and its reduced form. (fig. 3.1 (a) and (b) are acquired by Mr. Algar Raja.)

Redox reactions equations



3.1.2 Characterisation of photoanode: Titanium Nitride

The photoanode chosen was titanium nitride (TiN) mainly because of its stability and corrosion resistance in a variety of aggressive electrolytes which is usually encountered in typical battery systems and its decent conductivity. X-ray diffraction (XRD) pattern of TiN, Figure 3.2a, indicate a face centered cubic lattice which is known to be extremely corrosion resistant³³ making it a suitable candidate as an electrode material in aggressive electrolytes often encountered in battery systems. Its light absorption capability stems from the layer of titanium oxynitride (TiON) and titanium oxide phases, X-ray photoelectron spectroscopy (XPS) data, Figure 3.2b.³⁴⁻⁴¹ TiON is known to be visible light active and its coexistence with conducting TiN is expected to boost charge propagation and charge separation. UV-vis spectrum of TiN photoanode, Figure 3.2c shows a broad absorption band spanning the visible and UV regions. The Kubelka-Munk plot, figure 3.2d, with an integer for direct band show a linear region which can be extrapolated to a band gap equal to 2.3 eV, to the region where solar power is intense making it ideal for light harvesting. Mott-Schottky plot, figure 3.2e, show a positive slope suggesting its n-type characteristics and the carrier density calculated from the slope is found to be $3.37 \times 10^{19} \text{ cm}^{-3}$ suggesting a decent dopant density. The flat band potential (E_{fb}) extracted from the linear region by extrapolating it to potential axis is found to be -1.0 V vs. SHE. From the equation 2.14 the conduction band is found to be at -1.02 V vs. SHE which in turn is -3.42 eV with respect to the vacuum level (Figure 3.2f). The valence band position of TiN from the obtained band gap of 2.3 eV is -5.72 eV with respect to the vacuum level which corresponds to 1.28 V w.r.t SHE. The band diagram of TiN is shown in figure 3.2f in comparison with PBA electrode. semiconductor relevant parameters of TiN photoanode is shown in table 3.1.

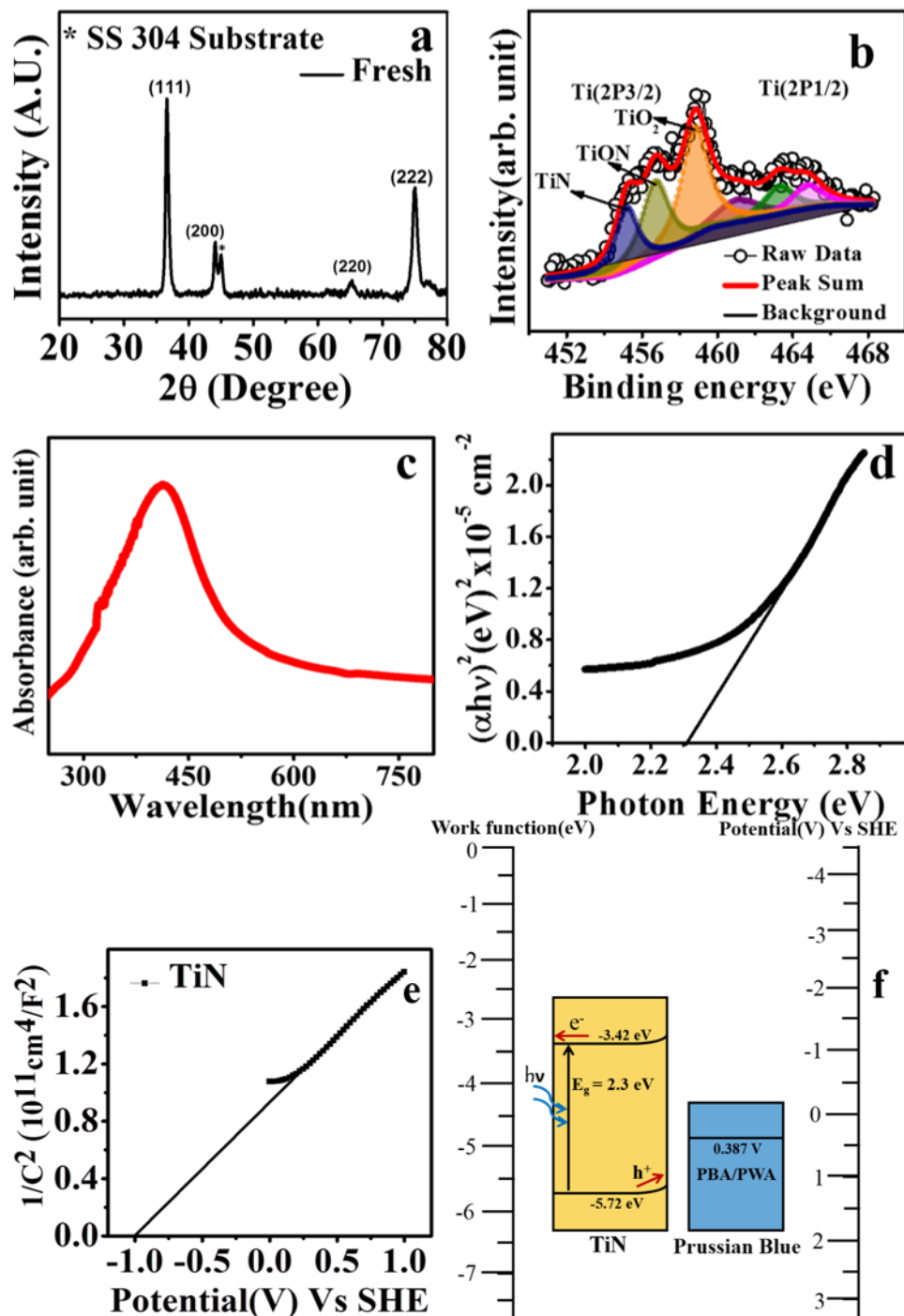


Figure 3.2. a) XRD pattern, (b) XPS spectrum, (c) UV-vis spectrum, (d) Kubelka-Munk plot, (e) Mott-Schottky plot and (f) Band diagram of TiN.(fig. 3.2 (b) and (e) are acquired by Dr. Ravikumar.)

3.1.3 Characterisation of photocathode: MgFeO

Photocathode, Mg-doped Fe₂O₃ (MgFeO) was fabricated by electrodeposition techniques with and without Mg²⁺ precursor (see experimental section for more details). Firstly the dopant concentration was optimized to get a decent absorption in the visible region. The UV-vis spectra of MgFeO for various molar % of Mg are shown in figure 3.3a. Generally the material exhibit broad absorption in the visible to UV regions making it a potential candidate for light harvesting. When the percentage of Mg in the deposition solution is 15%, the UV-vis absorption band show an obvious increase in the visible and UV regions, suggesting an improvement in its absorption capability due to Mg²⁺ incorporation, however a further increase of precursors in the electrodeposition bath, decreased the absorption capability possibly because of the blocking of Fe₂O₃ surface by Mg ion making less surface available for light absorption. The Tauc plot (Figure 3.3b) with an integer ½ for direct band gap indicate a band gap of 2 eV when the amount of Mg²⁺ concentration was 15%, making it a potential candidate for light harvesting since it fall near the region where solar power is intense. XRD data, figure 3.3c, show almost unchanged diffraction patterns when the amount of Mg is increased, suggesting a substitutional doping without affecting the rhombohedral (hexagonal) crystal structure of Fe₂O₃. No additional diffraction patterns were evolved during Mg doping, indicating a pure phase without impurities. The charging profiles of the battery species with different percent of MgFeO in the ambient light, visible light and UV-vis light demonstrate that 15% of MgFeO outperform other compositions (figure 3.3d). Mott-Schottky plot of 15% MgFeO, figure 3.3e, suggests a negative going slope as opposed to a positive going slope observed for pure Fe₂O₃ indicating that incorporation of Mg²⁺ ions induces p-type character to Fe₂O₃. Therefore this substitutional doping of Mg is quintessential for Fe₂O₃ to act as a photocathode thereby making it a potential photocharging electrode. SEM with energy-dispersive X-ray spectroscopy (EDS), figure 3.4a show the presence of particles with Mg dopants, and Mg % show an obvious increase when the amount of Mg in the deposition solution is increased (Table 3.2). The percent of Mg determined from EDS when the deposition solution contained 15% of Mg was 1.84% and the reason for disparity is currently under investigation. Based on UV-vis studies, Mott-Schottky analysis and charging profiles 15% Mg in the deposition solution (1.84% dopant) is taken as the optimal

candidate as photocathode material. The carrier concentration extracted from the slope in figure 3.3e for 15% MgFeO is found to be $1.78 \times 10^{18}/\text{cm}^3$ suggesting a decent dopant level. The valence band level is found to be 1.06 V vs. SHE (table 3.1) which is -5.5 eV with respect to the vacuum level. The conduction band level calculated based on the band gap and valence band level is -3.5 eV with respect to the vacuum level which is suitably positioned to receive electrons from discharged PBA (figure 3.4b). The band diagram of

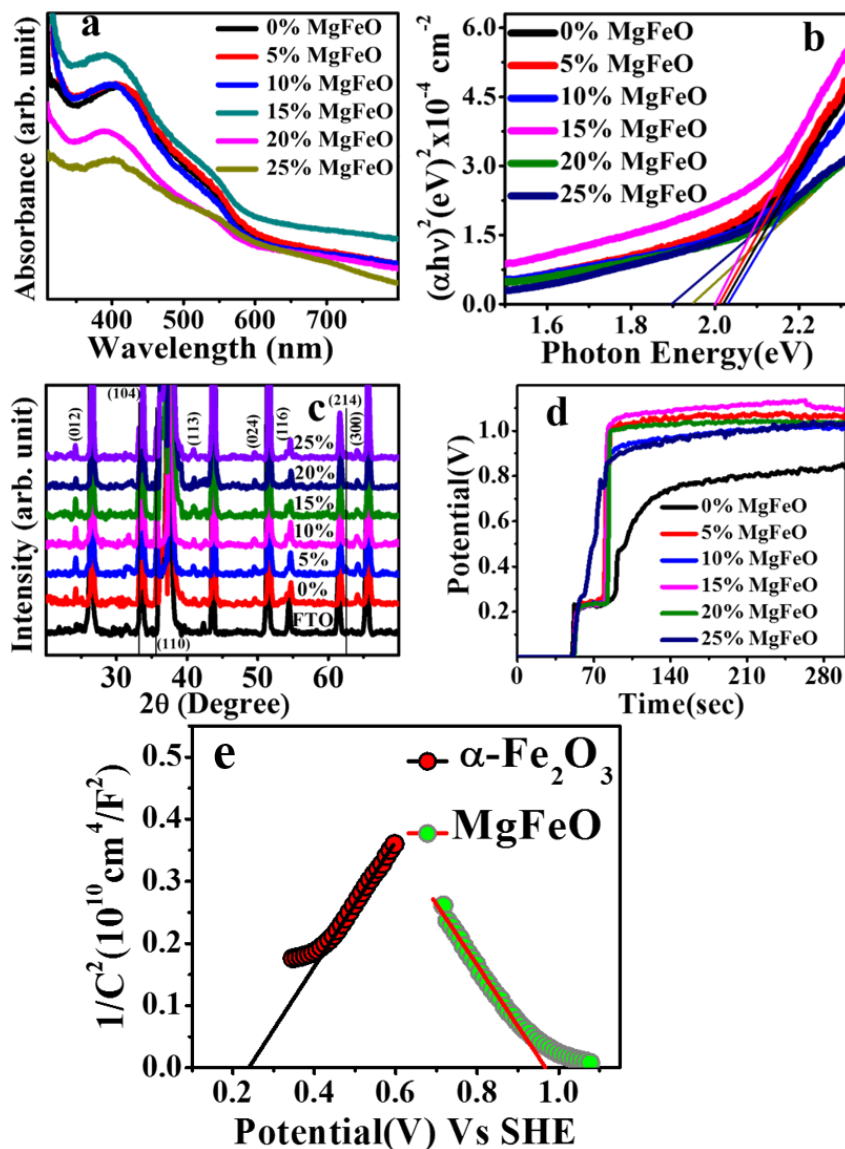
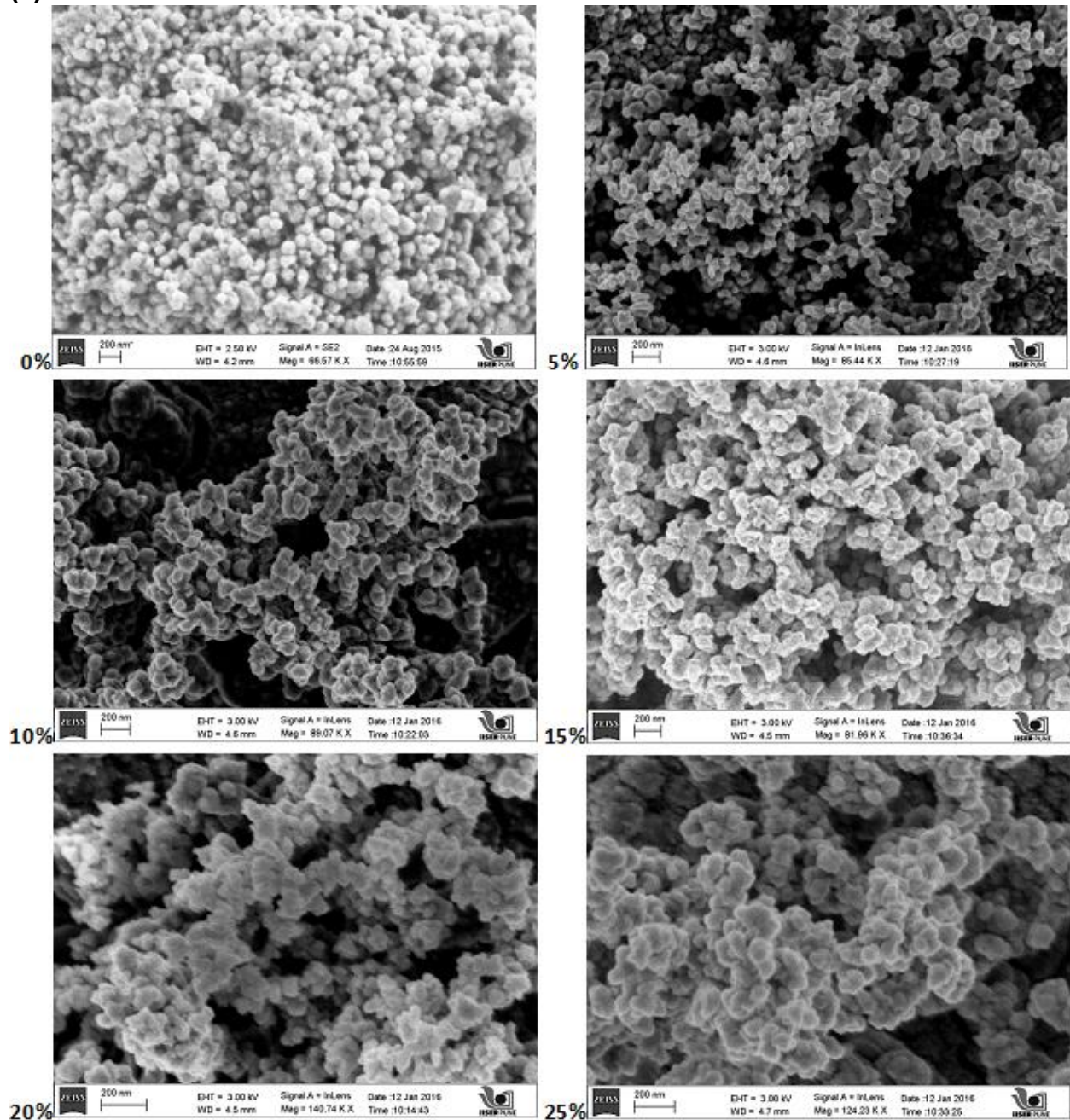


Figure 3.3. (a) UV-Vis spectra, (b) Tauc plot and (c) XRD patterns for various molar % of Mg, (d) charging chemistry in visible light for different % of MgFeO and (d) Mott-Schottky plot of 15% MgFeO along with α -Fe₂O₃.

15% MgFeO photocathode is shown in Figure 3.4b, along with battery electrode demonstrating that downward band bending of MgFeO rectifies the electron flow towards the interface of MgFeO electrode by accepting electrons from discharged PBA (PWA), thereby photo charging the battery electrode. Semiconductor relevant parameters are given in table 3.1.

(a)



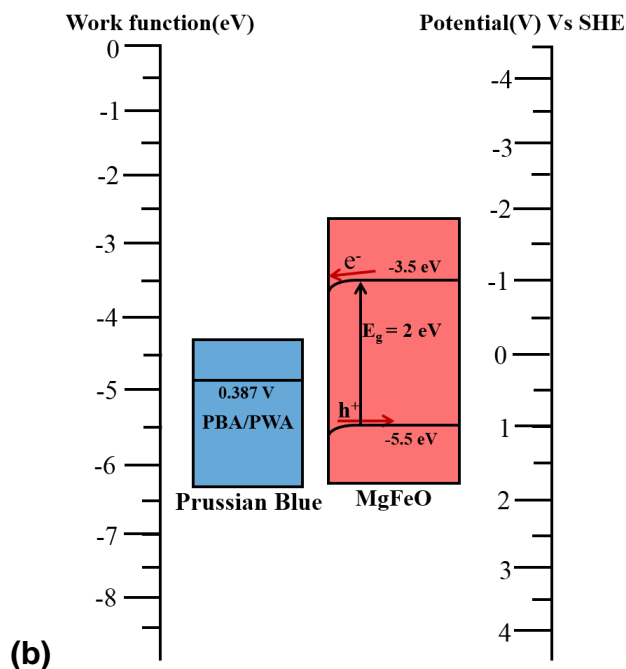


Figure 3.4. (a) FESEM of MgFeO for different molar % (Mg/(Mg+Fe)) in electrodeposition solution and (b) the band diagram of 15% MgFeO photocathode.

Table 3.1 : Semiconductor relevant characteristics of battery electrodes.

Electrode	Flat-band potential	Conduction band	Valance Band	Depletion layer width	Built-in Potential	Schottky-Barrier Height
TiN	-3.416 eV	-3.420 eV	-5.720 eV	3.84 nm	0.0997 V	0.104 V
α -Fe ₂ O ₃	-4.670 eV	-4.590 eV	-6.610 eV	36.23 nm	0.084 V	0.344 V
MgFeO	-5.410 eV	-3.500 eV	-5.500 eV	70.20 nm	0.099 V	0.192 V

Table 3.2 : Atomic % of Mg in electrodeposition solution compared with the EDS data

Atomic percentage of Mg in electrolyte	Atomic percentage of Mg in MgFeO Electrode
0%	0.00%
5%	0.12%
10%	0.90%
15%	1.84%
20%	2.69%
25%	3.54%

3.2 Solar battery architect and charge discharge behavior

The architectural arrangement of the solar battery is shown in figure 2.1 and it consists of a TiN photoanode, PBA battery electrode and 15% MgFeO photocathode. It was observed that when TiN photoanode was short circuited to PBA battery electrode in ambient light, immediate bleaching of PBA to its reduced form indicating that TiN can reduce PBA to its reduced form. When left at the open circuit no observable changes occurred, however within 15 min of its shortcircuiting to MgFeO photocathode the original PBA cathode was restored suggesting the MgFeO photocathode can restore the battery active species. This suggests that in presence of light, TiN can act as a source of electrons and MgFeO can act as a source of holes for accepting electrons from discharged PBA. The discharge behavior of TiN PBA electrode is shown in figure 3.5a under different conditions of light. It should be noted that no external bias was applied to charge the battery and after every discharge the battery electrode was short circuited to the photocathode (MgFeO) for recovery. In the dark, no discharge capacity was observed however a noticeable capacity was observed in the ambient light. When intentionally shined with visible light the discharge plateau and discharge capacities were improved. In UV-vis light further improvement in discharge capacity and discharge plateau were observed. All these demonstrate that the discharge chemistry is light driven. Associated reactions are shown in equation 3.3 – 3.8 and it consists of light assisted generation of electron hole pairs and the pumping of electrons to PBA causing the reduction of high spin Fe^{3+} transition metal ion with concomitant metal ion insertion for charge balance. UV-vis spectra, figure 3.5b, during the discharge with TiN photoanode clearly indicate the transition from opaque to transparent state confirming the transformation of high spin Fe^{3+} to low spin Fe^{2+} . The generated holes are used for O_2 evolution reaction which is observed from the bubbles observed on the TiN photoanode during the discharge chemistry (Figure 3.5c). At pH=0 the valence band position have just the energy to oxidise H_2O , however at pH=3 (as in the present electrolyte) oxidation of water to O_2 is expected to be accelerated. The energy level diagram (figure 3.2f) with respect to PBA/PWA redox levels suggest that the depletion region in n-type TiN semiconductor spatially separate the electrons and holes and generated photo-electrons travel through the external circuit to the battery cathode during the discharge reaction.

The charge behavior, figure 3.5d & 3.5e, of the discharged PBA electrode is investigated with and without MgFeO photocathode. When a discharged battery electrode was short circuited to MgFeO in the presence of light the original battery electrode was restored as seen from the recovery of battery open circuit voltage (OCV), figure 3.5d. The OCV profiles of TiN photoanode and battery electrode after first discharge, Figure 3.5e, show that in the absence of photocathode, the OCV marginally regained only to 0.45V even after 1000sec and did not reveal a noticeable change during illumination. In the absence of photocathode, the discharge capacity after a waiting period of 1000 seconds after the 1st discharge was abysmal, figure 3.5f, indicating the battery cannot self-recover. However when the battery electrode after 1st discharge was short circuited to Mg-Fe₂O₃ in visible light, figure 3.5d, a sudden rise to 1.1 V can be seen and the OCV was maintained at this voltage even after the MgFeO was disconnected from the circuit and the subsequent discharge revealed identical capacity as in the first discharge (figure 14f). In the dark OCV regained only to 0.6 V (figure 3.5d) and the subsequent discharge did not yield appreciable capacity (figure 3.5a & 3.5d). All these indicate that MgFeO can charge the discharged battery electrode in the presence of light. When the short circuiting of discharged battery electrode to MgFeO was done in the presence of ambient and UV-vis light, OCV regained to 0.95 V and 1.2 V respectively proving that charge chemistry is light driven, figure 3.5d. UV-vis spectra, figure 3.6a, of battery electrode during the charge chemistry show the reverse of what observed with TiN demonstrating that battery electrode can recover to the original state during the charge chemistry in the presence of light. The transparent electrode changed to opaque on short circuiting to MgFeO suggesting that high spin redox Fe³⁺ is restored by the oxidation of low spin Fe²⁺ with concomitant metal ion expulsion. XRD data of the battery electrode, figure 15b, before discharge and after charge show identical patterns clearly demonstrating that battery charged state is recovered on short circuiting to photocathode and the charge chemistry is light driven. The charge reactions involve pumping of electrons from PWA to the valence band of MgFeO as the depletion region in p type photocathode spatially separate the electron and hole with the photo generated holes moving away from the interface. Therefore the valence band position of MgFeO is conducive to accept electrons from PWA discharged battery electrode and the generated electrons on MgFeO are used for

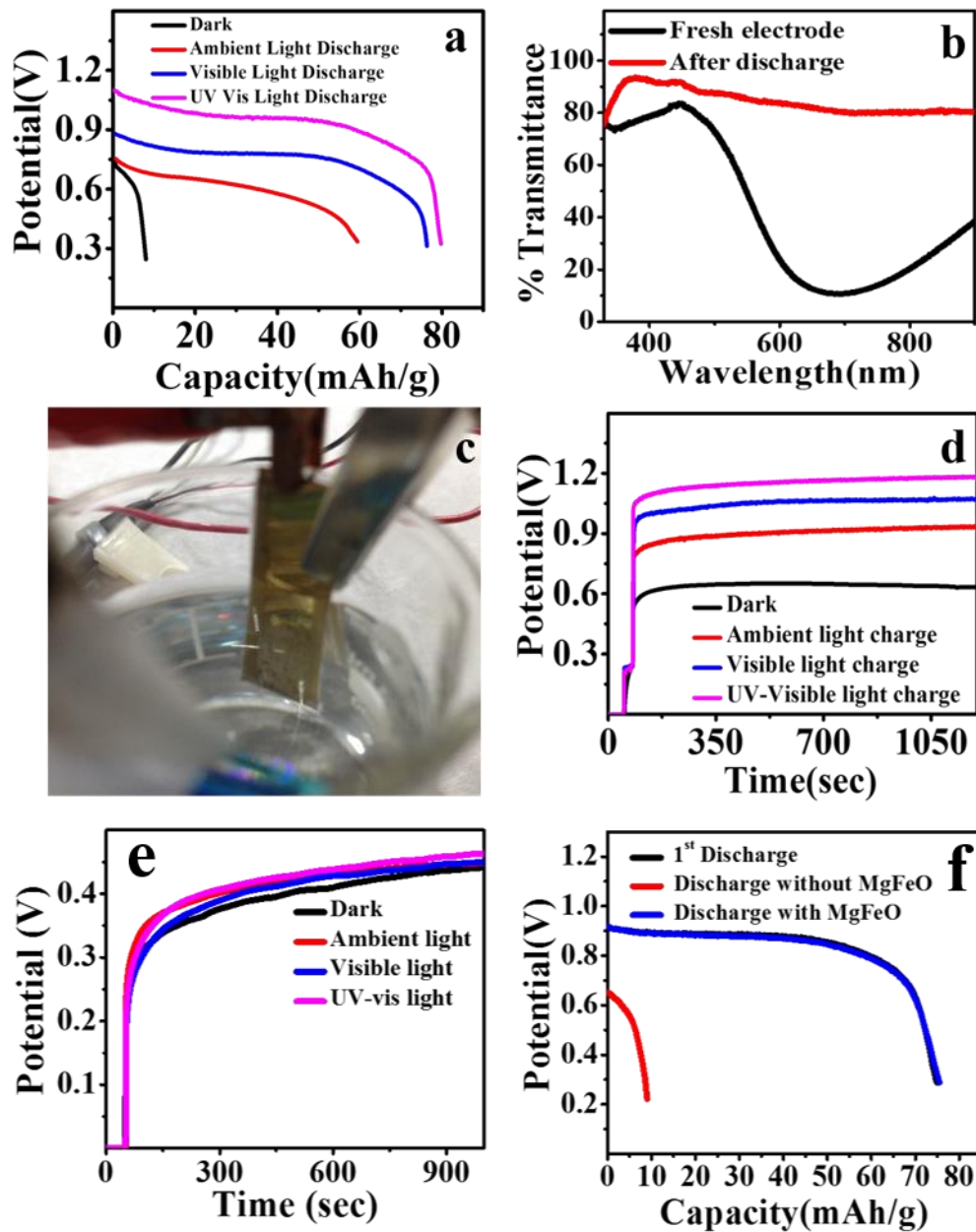


Figure 3.5. (a) Discharge behavior of TiN PBA electrodes under different conditions of light, (b) UV-vis spectra of PBA electrode before discharge and after charge, (c) O₂ bubbles observed on the TiN photoanode during the discharge chemistry, (d) charge behavior of TiN PBA electrodes under different conditions of light and (e) charge profile in the absence of photocathode. (f) 1st and 2nd discharge in visible light in the absence and presence of photocathode. (fig. 3.5 (a), (c) and (f) are acquired by Dr. Ravikumar.)

H₂ evolution reactions. To remove the ambiguity of oxygen reduction reactions as a possible reaction instead of proton reduction we carried out charge discharge chemistry

in visible light in inert atmosphere and the results, figure 3.7, suggests that discharge-charge chemistry is independent of the presence of oxygen excluding this possibility. The energy diagram of the complete solar battery with all the architectural components and possible reactions are shown in figure 3.8.

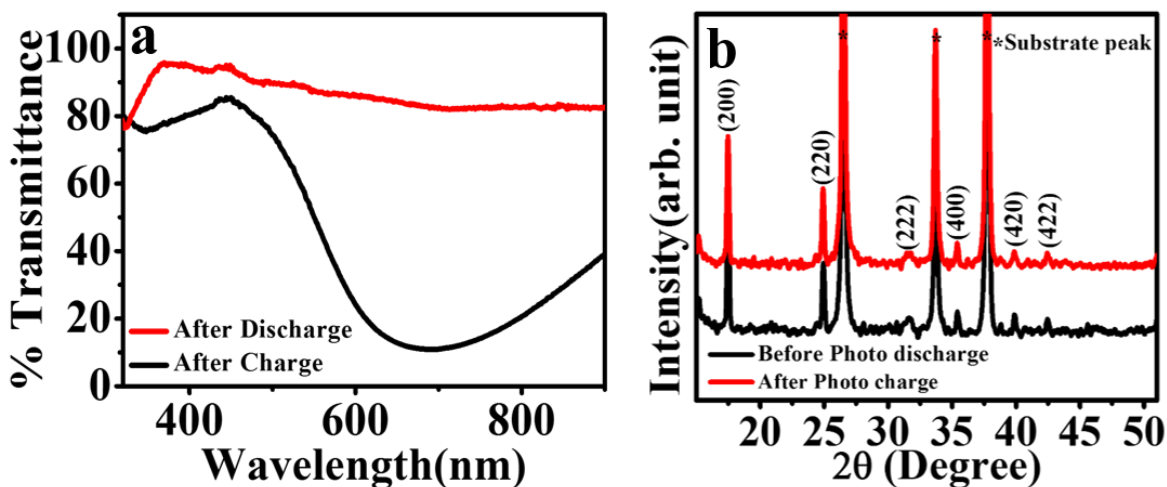
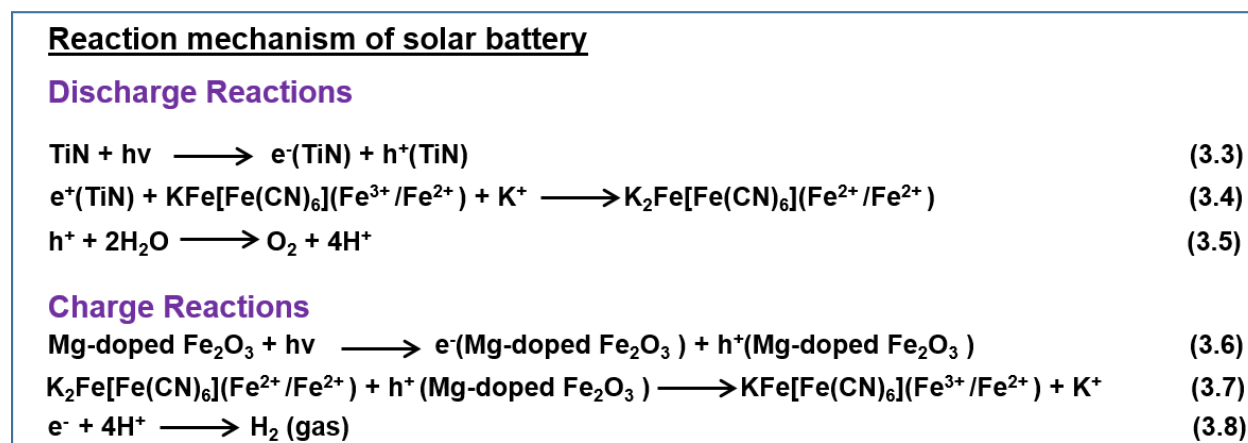


Figure 3.6. (a) UV-vis spectra and (b) XRD of PBA during charge chemistry with the photocathode.

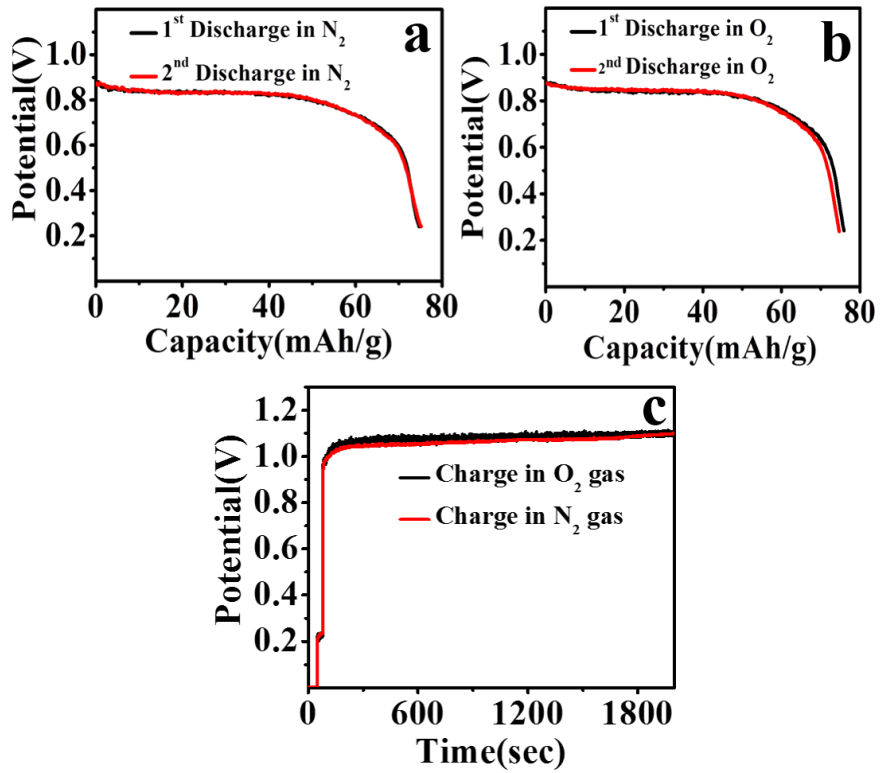


Figure 3.7. Discharge behavior of solar battery in (a) N_2 and (b) O_2 atmosphere showing identical discharge capacities. (b) Charge behavior of solar battery in the presence of nitrogen and oxygen. (fig. 3.7 (a) and (b) are acquired by Dr. Ravikumar.)

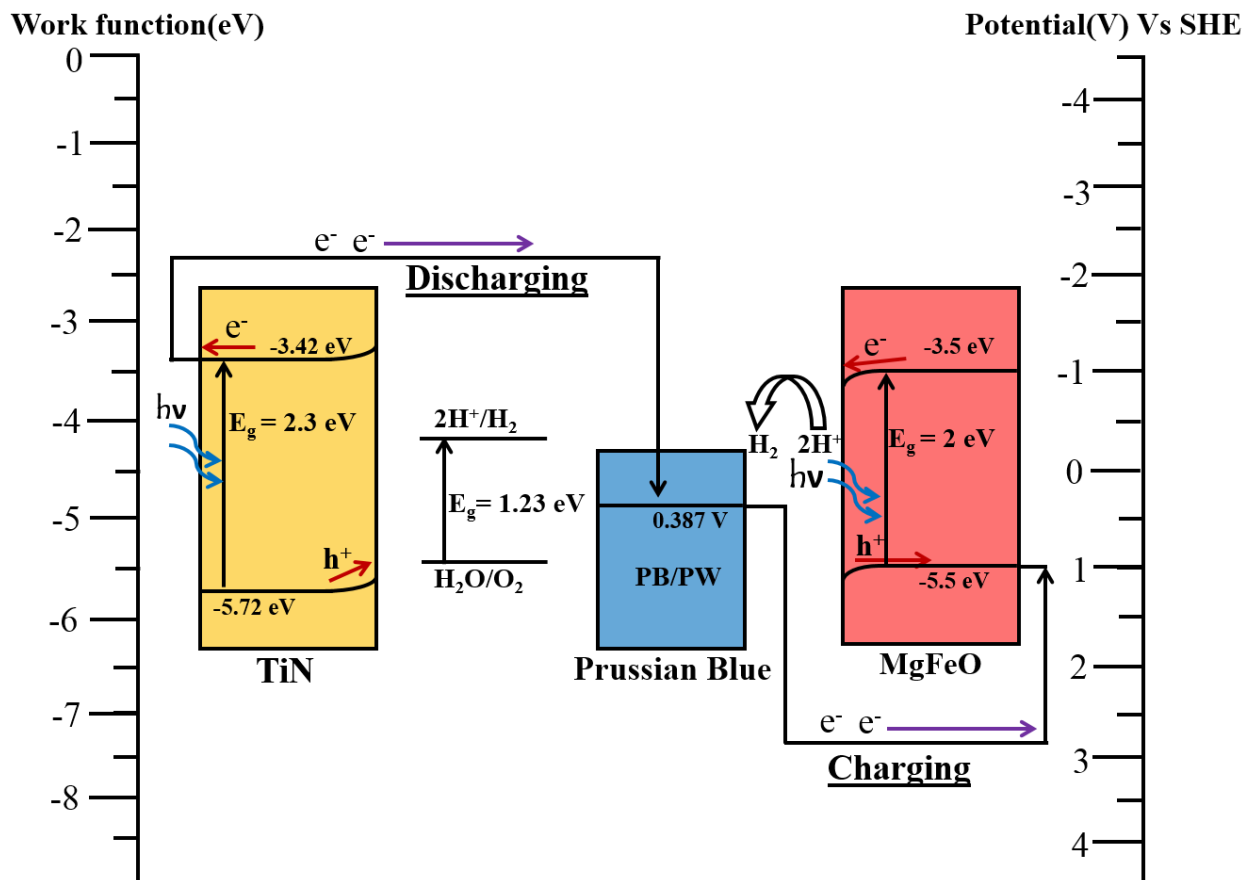


Figure 3.8. Energy level diagram of various architectural components of the proposed solar battery.

3.3 Stability and cycling

Stability and cyclability of the solar battery, during multiple charge discharge cycles are investigated. The XRD patterns of TiN during extended cycling show identical patterns for 250 cycles as shown in figure 3.9a demonstrating its decent stability. TiN is known to be corrosion resistant in a variety of electrolyte and this could be the responsible factor for the extended cyclability of the photoanode³⁴. The discharge capacity during extended cycling is followed by photocharging the battery electrode with the photocathode after every discharge. For over 250 cycles, decent stability and cyclability are observed, as shown in figures 3.9b, 3.9c & 3.9d, and it retained almost 90% of its capacity in different light conditions demonstrating extended cyclability. The discharge capacity plot in visible, figure 3.9c, and UV-vis light, figure 3.9d, show improved capacity by maintaining extended cyclability indicating the stability of battery architectural components in visible

and UV vis light. . UV-vis data of battery electrode show attenuation between opaque and transparent state during the photo charge and photo discharge respectively, figure 3.10a for over 250 cycles, demonstrating again its extended cyclability and stability. Further XRD data of the battery electrode after every cycle (discharge and charge), figure 3.10b, show nearly identically profiles during extended cycling, affirming the extended stability of the battery electrode. Photocathode stability can be seen from the XRD data figure 3.10c during extended cycling. The OCV profiles during the extended cycling using the photocathode in ambient light , visible light, and UV-vis light (figure 3.11a, 3.11b & 3.11c) demonstrate further the decent stability and cyclability of the photocathode.

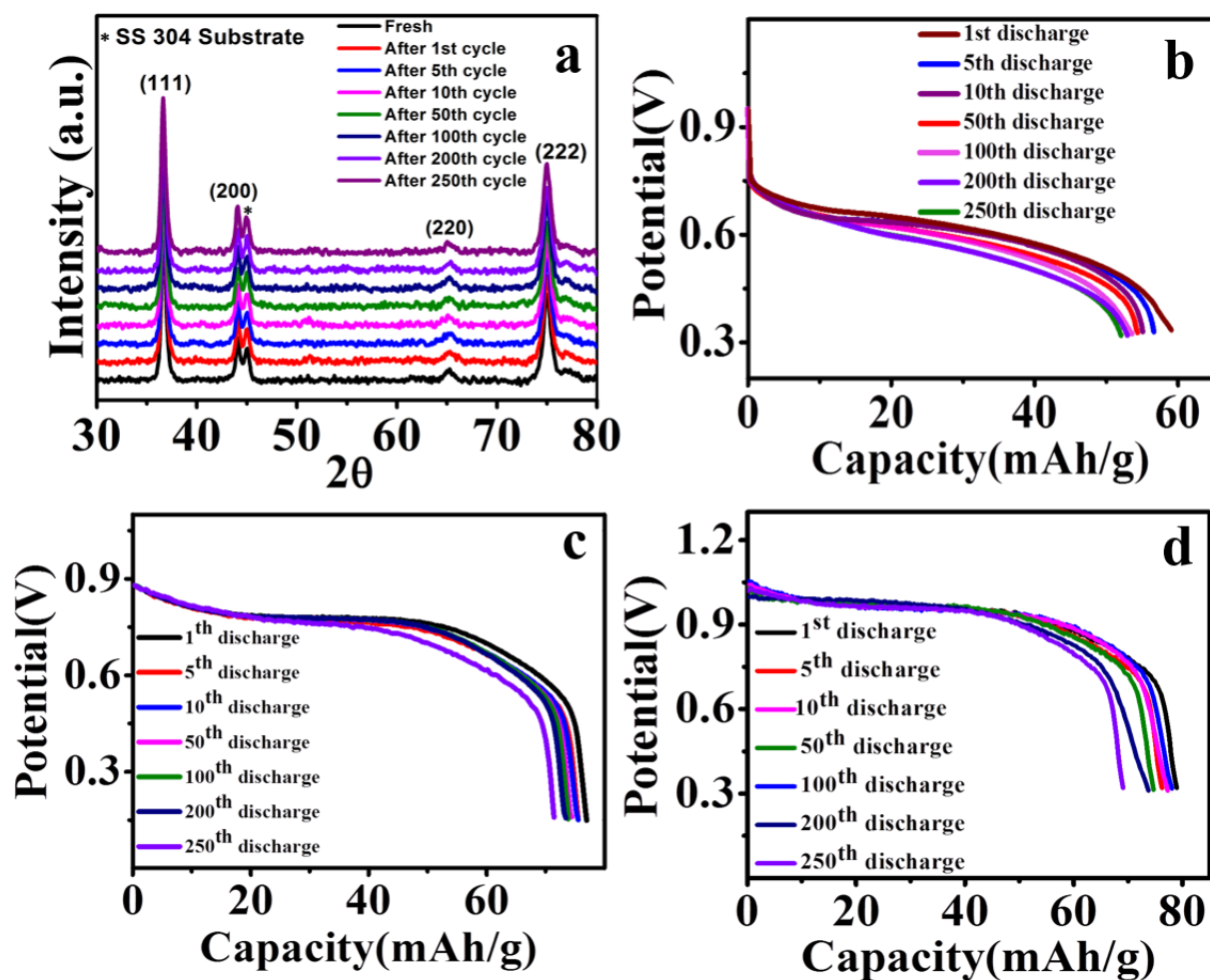


Figure 3.9. (a) XRD of TiN for 250 cycle during photodischarge. Discharge cycles of solar battery (b) in ambient light, (c) in visible light and (d) UV-vis light for 250 cycles. (fig. 3.9 (b), (c) and (d) are aquired and processed by Dr. Ravikumar.)

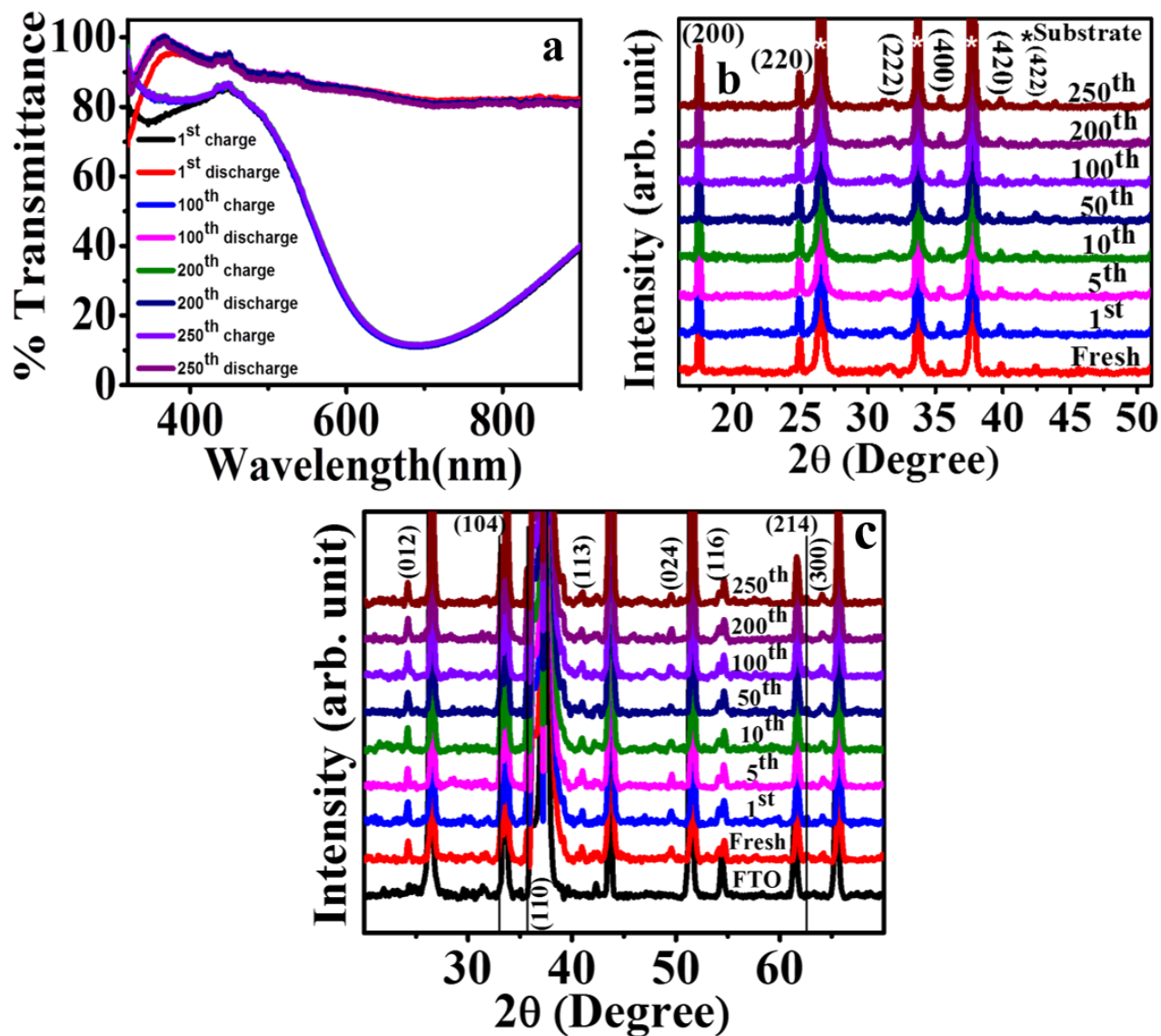


Figure 3.10. (a) UV-VIS spectra and (b) XRD of PBA for 250 cycles during extended photodischarge and photocharge. (c) XRD of photocathode for 250 cycles during photocharge.

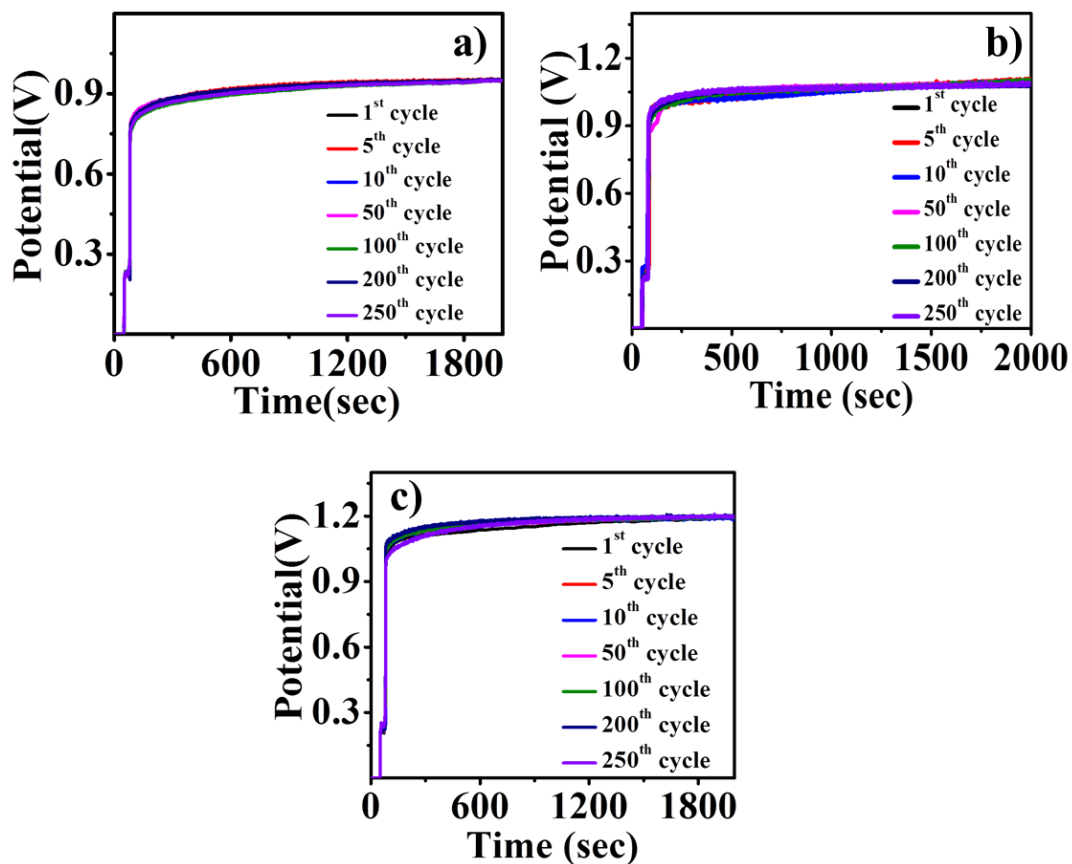


Figure 3.11: Charge profiles of the solar battery during extended cycling in (a) ambient light, (b) visible light and (c) UV-Vis light.

4. CONCLUSIONS

In essence we have fabricated a metal ion solar battery where the discharge and charge reactions are completely light driven. Light assisted discharge reactions stimulate the reduction of high spin transition metal ions with concomitant metal ion insertion in the battery electrode. As the electron flow in MgFeO photocathode is rectified by the downward band bending, the discharged battery electrode is forced to pump electrons to the holes in the valence band of photocathode during photocharging with a concomitant metal ion deinsertion reaction at the battery electrode. The solar battery could be cycled multiple times without an external bias while maintaining almost 90% discharge capacity at the end of 250 cycles.

The difficulty of the present architect is the longer charging time encountered during photocharge. It should be noted that efforts are going on in our laboratory to bring down the charging time and to achieve this goal, we propose engineering the photocathode surface by hydrogen evolution catalysts like MoS₂, Ni₃S₂ etc. which is expected to increase the efficiency of electron hole separation as hydrogen evolution is a kinetically controlled reaction.

Nevertheless the strategy of combining light harvesting component and energy storing component in the same device leads to a practical and economical device as it decrease the complexity of solution and electrode chemistries existing when they occupy as different modules. Further ambient light assisted discharge and charge reactions are demonstrated making it ideal for harvesting indoor lighting, household lighting etc.

5. REFERENCES

1. Lelieveld, J.; Crutzen, P. J.; Ramanathan, V.; Andreae, M. O.; Brenninkmeijer, C. M.; Campos, T.; Cass, G. R.; Dickerson, R. R.; Fischer, H.; de Gouw, J. A.; Hansel, A.; Jefferson, A.; Kley, D.; de Laat, A. T. J.; Lal, S.; Lawrence, M. G.; Lobert, J.M.; Mayol-Bracero, O.L.; Mitra, A. P.; Novakov, T.; Oltmans, S. J.; Prather, K. A.; Reiner, T.; Rodhe, H.; Scheeren, H. A.; Sikka, D.; Williams, J. The Indian Ocean experiment: widespread air pollution from South and Southeast Asia. *Science*. **2001**, *291(5506)*, 1031–1036.
2. Hansen, J. E. A slippery slope: How much global warming constitutes “dangerous anthropogenic interference”? An editorial essay. *Climatic Change*. **2005**, *68(3)*, 269–279.
3. Doney, S. C.; Fabry, V. J.; Feely, R. A.; Kleypas, J. A. Ocean Acidification: The Other CO₂ Problem. *Annual Review of Marine Sci.* **2009**, *1(1)*, 169–192.
4. Riebesell, U.; Zondervan, I.; Rost, B.; Tortell, P. D.; Zeebe, R. E.; Morel, F. M. Reduced calcification of marine plankton in response to increased atmospheric CO₂. *Nature*. **2000**, *407(6802)*, 364–7.
5. Spicer, J. I.; Raffo, A.; Widdicombe, S. Influence of CO₂-related seawater acidification on extracellular acid–base balance in the velvet swimming crab *Necora puber*. *Marine Biology*. **2007**, *151(3)*, 1117–1125.
6. Alstrum-Acevedo, J. H.; Brennaman, M. K.; Meyer, T. J. Chemical approaches to artificial photosynthesis. *Inorganic Chemistry*. **2005**, *44(20)*, 6802–6827.
7. Barbir, F. *PEM Fuel cells theory and practice*, 2nd ed.; Elsevier, 2013; p. 397-398.
8. Jost, K.; Dion, G.; Gogotsi, Y. Textile energy storage in perspective. *J. Mater. Chem. A*. **2014**, *2(28)*, 10776–10787.
9. Grätzel, M. Photovoltaic and photoelectrochemical conversion of solar energy. *Philosophical Transactions. Series A, Mathematical, Physical, and Engineering Sciences*. **2007**, *365(1853)*, 993–1005.
10. Hebrink, T. J. *Third Generation Photovoltaics*, 1st ed.; InTech: Rijeka, Croatia, 2012; p. 184.

11. Kleiman-Shwarsctein, A.; Hu, Y.; Forman, A. J.; Stucky, G. D.; McFarland, E. W. Electrodeposition of α -Fe₂O₃ Doped with Mo or Cr as Photoanodes for Photocatalytic Water Splitting. *The Journal of Physical Chemistry C*. **2008**, *112*(40), 15900–15907.
12. Karyakin, A. A. Prussian blue and its analogues: Electrochemistry and analytical applications. *Electroanalysis*. **2001**, *13*(10), 813–819.
13. Kleiman-Shwarsctein, A.; Huda, M. N.; Walsh, A.; Yan, Y.; Stuckyst, G. D.; Hu, Y. S.; McMland, E. W. Electrodeposited aluminum-doped α -Fe₂O₃ photoelectrodes: Experiment and theory. *Chemistry of Materials*. **2010**, *22*(2), 510–517.
14. Mabbott, G. A. An introduction to cyclic voltammetry. *Journal of Chemical Education*. **1983**, *60*(9), 697–702.
15. Li, Y.; Chen, S. M. The electrochemical properties of acetaminophen on bare glassy carbon electrode. *International Journal of Electrochemical Science*. **2012**, *7*(3), 2175–2187.
16. Fouzri, A.; Boukadhaba, M. A.; Oumezzine, M.; Sallet, V. Structural properties and morphology of Zn_(1-x)Cd_xO solid solution grown on ZnO and C-plane sapphire substrate. *Thin Solid Films*. **2012**, *520*(7), 2582–2588.
17. Clausen, B. S. Combined (Q) EXAFS/XRD: Technique and applications. *Catalysis Today*. **1998**, *39*(4), 293–300.
18. Tumuluri, A.; Naidu, K. L.; Raju, K. C. J. Band gap determination using Tauc's plot for LiNbO₃ thin films. *Int. J. ChemTech. Res.* **2014**, *6*(6), 3353–3356.
19. Albery, W. J.; O'Shea, G. J.; Smith, A. L. Interpretation and use of Mott-Schottky plots at the semiconductor/electrolyte interface. *Journal of the Chemical Society, Faraday Transactions*. **1996**, *92*(20), 4083.
20. Butler, M. A. Photoelectrolysis and physical properties of the semiconducting electrode WO₂. *Journal of Applied Physics*. **1977**, *48*(5), 1914–1920.
21. Shen, S.; Zhou, J.; Dong, C. L.; Hu, Y.; Tseng, E. N.; Guo, P.; Mao, S. S. Surface engineered doping of hematite nanorod arrays for improved photoelectrochemical water splitting. *Scientific Reports*. **2014**, *4*, 6627.

22. Patsalas, P.; Logothetidis, S. Optical, electronic, and transport properties of nanocrystalline titanium nitride thin films. *Journal of Applied Physics*. **2001**, *90*(9), 4725–4734.
23. Chawla, J. S.; Zhang, X. Y.; Gall, D. Effective electron mean free path in TiN(001). *Journal of Applied Physics*. **2013**, *113*(6), 1–6.
24. H. Peng and S. Lany, Semiconducting transition-metal oxides based on d^5 cations: Theory for MnO and Fe₂O₃, *Phys. Rev. B*. **2012**, *85*(20), 230- 237.
25. Neff, D. Electrochemistry of Polynuclear Transition Metal Cyanides : Prussian Blue and Its Analogues. *Accounts of Chemical Research*. **1986**, *19*(17), 162–168.
26. Wurfel, P. *Physics of Solar cells: from basic principles to advanced concepts*, 2nd ed.; Wiley-Vch, 2009; p. 43- 66.
27. Hara, S.; Tanaka, H.; Kawamoto, T.; Tokumoto, M.; Yamada, M.; Gotoh, A.; Uchida, H.; Kurihara, M.; Sakamoto, M. Electrochromic Thin Film of Prussian Blue Nanoparticles Fabricated using Wet Process. *Japanese Journal of Applied Physics*. **2007**, *46*(38), 945–947.
28. Winter, M.; Brodd, R. J. What are batteries, fuel cells, and supercapacitors? *Chemical Reviews*. **2004**, *104*(10), 4245–4269.
29. Lu, Y.; Wang, L.; Cheng, J.; Goodenough, J. B. Prussian blue : a new framework of electrode materials for sodium batteries. *Chem. Comm*. **2012**, *48*, 6544–6546.
30. Neff, D. Electrochemistry of Polynuclear Transition Metal Cyanides : Prussian blue and Its Analogues. *Accounts of Chemical Research*. **1986**, *19*(17), 162–168.
31. Wang, L.; Song, J.; Qiao, R.; Wray, L. A.; Hossain, M. A.; Chuang, Y. D.; Yang, W.; Yuhao L. Y.; Evans, D.; Lee, J. J.; Vail, S.; Zhao, X.; Nishijima, M.; Kakimoto, S.; Goodenough, J. B. Rhombohedral Prussian white as cathode for rechargeable sodium-ion batteries. *Journal of the American Chemical Society*. **2015** *137*(7), 2548–2554.
32. Tarascon, J. M.; Armand, M. Issues and challenges facing rechargeable lithium batteries. *Nature*. **2001**, *414*, 359–367.
33. Starosvetsky, D.; Gotman, I. TiN coating improves the corrosion behavior of superelastic NiTi surgical alloy. *Surface and Coatings Tech*. **2001**, *148*, 268–276.

34. Asahi, R.; Morikawa, T.; Ohwaki, T.; Aoki, K.; Taga, Y. Visible-light photocatalysis in nitrogen-doped titanium oxides. *Science*. **2001**, *293*, 269-271.
35. Carp, O. Photoinduced reactivity of titanium dioxide. *Progress in Solid State Chemistry*. **2004**, *32(1-2)*, 33–177.
36. Ihara, T.; Miyoshi, M.; Iriyama, Y.; Matsumoto, O.; Sugihara, S. Visible-light-active titanium oxide photocatalyst realized by an oxygen-deficient structure and by nitrogen doping. *Applied Catalysis B: Environmental*. **2003**, *42(4)*, 403–409.
37. Irie, H.; Watanabe, Y.; Hashimoto, K.; Nitrogen-Concentration Dependence on Photocatalytic Activity of $\text{TiO}_{2-x}\text{N}_x$ Powders. *J. Phys. Chem. B*. **2003**, *107*, 5483-5486.
38. Kim, H. G.; Hwang, D. W.; Lee, J. S. An Undoped Single-Phase Oxide Photocatalyst Working under Visible Light. *J. Am. Chem. Soc.* **2004**, *126(29)*, 8912–8913.
39. Kim, J. Y.; Kim, S. H.; Lee, H. H.; Lee, K.; Ma, W.; Gong, X.; Heeger, A. J. New Architecture for High-Efficiency Polymer Photovoltaic Cells Using Solution-Based Titanium Oxide as an Optical Spacer. *Advanced Materials*. **2006**, *18(5)*, 572–576.
40. Morikawa, T.; Asahi, R.; Ohwaki, T., Aoki, K.; Taga, Y. Band-Gap Narrowing of Titanium Dioxide by Nitrogen Doping. *Japanese Journal of Applied Phys.* **2001**, *40(Part 2, No. 6A)*, L561–L563.
41. Sakthivel, S.; Kisch, H. Photocatalytic and photoelectrochemical properties of nitrogen-doped titanium dioxide. *Chem. Phys. Chem.* **2003**, *4(5)*, 487–490.